

AFGL-TR-82-0027  
ENVIRONMENTAL RESEARCH PAPERS, NO. 765



# Improved Cloud Detection Utilizing Defense Meteorological Satellite Program Near Infrared Measurements

JAMES T. BUNTING  
ROBERT P. d' ENTREMONT

IRIA No. 51201 U  
 Contractor CRCA  
 Contract No. 1  
 Contract No. 2  
 Dept. Service 3  
 Sponsoring Agency CRCA  
 Pub. Date 1 82

1982

Approved for public release; distribution unlimited.

METEOROLOGY DIVISION PROJECT 6670  
**AIR FORCE GEOPHYSICS LABORATORY**  
HANSCOM AFB, MASSACHUSETTS 01731

**AIR FORCE SYSTEMS COMMAND, USAF**



This report has been reviewed by the ESD Public Affairs Office (PA)  
and is releasable to the National Technical Information Service (NTIS).

This technical report has been reviewed and  
is approved for publication.

  
\_\_\_\_\_  
DR. ALVA T. STAIR, Jr  
Chief Scientist

Qualified requestors may obtain additional copies from the  
Defense Technical Information Center. All others should apply  
to the National Technical Information Service.

Unclassified

SECURITY CLASSIFICATION OF THIS PAGE (When Data Entered)

REPORT DOCUMENTATION PAGE		READ INSTRUCTIONS BEFORE COMPLETING FORM
1. REPORT NUMBER AFGL-TR-82-0027	2. GOVT ACCESSION NO.	3. RECIPIENT'S CATALOG NUMBER
4. TITLE (and Subtitle) IMPROVED CLOUD DETECTION UTILIZING DEFENSE METEOROLOGICAL SATELLITE PROGRAM NEAR INFRARED MEASUREMENTS		5. TYPE OF REPORT & PERIOD COVERED Scientific. Interim.
		6. PERFORMING ORG. REPORT NUMBER ERP No. 765
7. AUTHOR(s) James T. Bunting Robert P. d'Entremont		8. CONTRACT OR GRANT NUMBER(s)
9. PERFORMING ORGANIZATION NAME AND ADDRESS Air Force Geophysics Laboratory (LYS) Hanscom AFB Massachusetts 01731		10. PROGRAM ELEMENT, PROJECT, TASK AREA & WORK UNIT NUMBERS 62101F 66700805
11. CONTROLLING OFFICE NAME AND ADDRESS Air Force Geophysics Laboratory (LYS) Hanscom AFB Massachusetts 01731		12. REPORT DATE 27 January 1982
		13. NUMBER OF PAGES 91
14. MONITORING AGENCY NAME & ADDRESS (if different from Controlling Office)		15. SECURITY CLASS. (of this report) Unclassified
		15a. DECLASSIFICATION/DOWNGRADING SCHEDULE
16. DISTRIBUTION STATEMENT (of this Report)  Approved for public release; distribution unlimited.		
17. DISTRIBUTION STATEMENT (of the abstract entered in Block 20, if different from Report)		
18. SUPPLEMENTARY NOTES		
19. KEY WORDS (Continue on reverse side if necessary and identify by block number) Near infrared sensors    Snow cover detection Visible sensors            Weather satellites Infrared sensors          Satellite imagery Cloud detection            Multispectral processing Cloud analysis		
20. ABSTRACT (Continue on reverse side if necessary and identify by block number)  Six different automated classifiers, three of which were suggested by previous studies, were tested on a special data base of DMSP SSC (near IR channel, 1.51 to 1.63 $\mu\text{m}$ ) and OLS (visible channel, 0.4 to 1.0 $\mu\text{m}$ , and IR channel, 10.2 to 12.8 $\mu\text{m}$ ). The classifiers were used to distinguish water clouds, ice clouds, snow cover, and other cloud-free surfaces. A test sample of 433 known cases was found with the aid of the AFGL Man-Computer Interactive Data Access System. The tests demonstrated that three of the automated classifiers could use the SSC channel to provide new information (snow		

DD FORM 1473  
1 JAN 73

Unclassified

SECURITY CLASSIFICATION OF THIS PAGE (When Data Entered)

Unclassified

SECURITY CLASSIFICATION OF THIS PAGE(When Data Entered)

20. Abstract (Continued)

cover and cloud phase) and also improve the overall accuracy of automated classification. These three classifiers were the Woronicz/AFGWC classifier, which uses only SSC and visible data, the classifier by Hunt and others, and a minimum distance type of classifier. The latter two classifiers use SSC, visible, and IR data. The three classifiers could all achieve accuracies over 90 percent, which were 10 to 16 percentage points better than the best reference classifiers using only visible and IR data.

Classification accuracies improved when the type of background, land or water, was independently known as in the current AFGWC automated cloud analysis program (3DNEPH). The accuracy also improved when IR temperature information was judiciously added to the SSC and visible reflectivities. Many of the clear/cloud and water cloud/ice cloud misclassifications occurred for small-scale clouds such as cumulus or cirrus which were mixed clear/cloud scenes in the coarse resolution (6 to 10 n mi) of the SSC sensor. Fewer misclassifications would be expected if the SSC channel were added to the OLS instrument.

Automated cloud analysis programs (3DNEPH) at the AFGWC could benefit from the use of an SSC channel. The new information of cloud phase is important since many Air Force operations are sensitive to water clouds, which tend to occur at low altitudes, have the worst transmission for electro-optical systems, and are often supercooled causing icing conditions. The multispectral processors using the SSC channel discriminate clouds from snow cover and may allow visible data to be processed for morning orbits. Therefore, the use of an SSC channel could substantially increase the amount of visible data used by the 3DNEPH.

Unclassified

SECURITY CLASSIFICATION OF THIS PAGE(When Data Entered)

## Preface

We had assistance and encouragement from many sources. We are particularly indebted to Major Robert C. Woronicz of AFGWC. Through his foresight, representative data from the SSC were processed and archived during early winter in 1979. Consequently, when the spacecraft had battery problems so that the SSC sensor was not available for the full extent of a planned evaluation, a useful data base could still be provided to us. We are also grateful to Mr. A. W. Kimball of Westinghouse Electric Corporation for providing information on the SSC and OLS sensors and to Mrs. Celeste Gannon for typing the manuscript.



## Contents

1. INTRODUCTION	9
2. NEAR IR PROPERTIES OF CLOUDS	10
3. DMSP IMAGERY DATA	18
3.1 Special Sensor C	18
3.2 OLS IR and Visible	23
3.3 Earth Location, Colocation, and Normalization	26
4. IMAGE ANALYSIS	31
4.1 Interactive Capabilities	31
4.2 Examples	37
5. AUTOMATED CLOUD CLASSIFICATION	51
6. RESULTS	61
7. OPTIONS FOR IMPROVED 3DNEPH	82
8. CONCLUSIONS	85
REFERENCES	89

## Illustrations

1. Atmospheric Transmittance for a Vertical Path to Space From Sea Level for Six Model Atmospheres	12
2. Average Spectral Radiance for 36 Cases of Cumulus, 32 Cases for Cirrus, and 56 Cases of Snow from Valovcin <sup>2</sup>	14
3. Calculated Cloud Reflectance as a Function of Optical Thickness and Single Scattering Albedo According to Blau and Hovis <sup>8</sup>	15
4. The Horizontal Extent of Data Provided by OLS and SSC Sensors in a Partial Orbit	20
5. Approximate Ground Resolution of SSC and OLS Data	21
6. SSC Data (Center Strip) and Colocated Visible (Left) and IR (Right) as They Appear on the AFGL McIDAS at a Resolution of About 6 nmi	32
7. Visible (Left Strip) and IR (Right) at 3 nmi Resolution as They Appeared on the McIDAS	33
8. SSC Data (Center) and Colocated Visible (Left) and IR (Right) for 8 December 1979	38
9. Visible (Left) and IR (Right) Data at 3 nmi for the Locations Shown in Figure 8	39
10. SSC Data (Center), Colocated Visible (Left), and IR (Right) for 18 December 1979	40
11. Visible (Left) and IR (Right) Data at 3 nmi for the Locations Shown in Figure 10	41
12. SSC Data (Center), Colocated Visible (Left), and IR (Right) for 17 December 1979	42
13. Visible (Left) and IR (Right) Data at 3 nmi for the Locations Shown in Figure 12	43
14. SSC Data (Center), Colocated Visible (Left), and IR (Right) for 27 December 1979	44
15. Visible (Left) and IR (Right) Data at 3 nmi for the Locations Shown in Figure 14	45
16. SSC Data (Center), Colocated Visible (Left), and IR (Right) for 17 December 1979	46
17. Visible (Left) and IR (Right) Data at 3 nmi for the Locations Shown in Figure 16	47
18. SSC Data (Center), Colocated Visible (Left), and IR (Right) for 11 December 1979	48
19. Visible (Left) and IR (Right) Data at 3 nmi for the Locations Shown in Figure 18	49
20. Decision Tree Suggested by Hunt et al <sup>4</sup> for Classifying Water Clouds, Ice Clouds, Snow Cover, and Other Cloud-Free Surfaces	52
21. Decision Tree Suggested by Kimball <sup>23</sup> for Discriminating Cloudy from Cloud-Free Surfaces Including Snow Cover	54

## Illustrations

22. Decision Matrix by Woronicz <sup>3</sup> (Dashed Lines) Modified to Our Normalized Values of SSC (Solid Lines)	55
23. Plots of Category Means in Three Dimensions (SSC, Visible, Infrared)	58
24. Decision Matrix for Visible and IR Data	60
25. Category Means (Overall Means) of SSC and Visible	65
26. Overall Means of SSC and Visible for Cases Over Water (Dark Circles) and for Cases Over Land (Open Circles)	65
27. Overall Means and Overall Average Standard Deviations of SSC and Infrared	66
28. Overall Means of SSC and Infrared for Cases Over Water (Dark Circles) and for Cases Over Land (Open Circles)	66
29. Overall Means and Overall Average Standard Deviations of Infrared and Visible	67
30. Overall Means of Infrared and Visible for Cases Over Water (Dark Circles) and for Cases Over Land (Open Circles)	67
31. Critical Thresholds and Modification of Hunt Decision Tree Based on Our Cases	73
32. Woronicz Matrix Modified for Land Backgrounds Only With the Clouds Region Divided into Separate Regions for Water Clouds and Ice Clouds	76
33. Woronicz Matrix Modified for Water Backgrounds Only With the Cloudy Region Divided into Separate Regions for Water Clouds and Ice Clouds	76

## Tables

1. Absorption Coefficient for Ice and Water vs Wavelength	12
2. Properties of Water Clouds, Ice Clouds, and Snow Cover	17
3. SSC Major System Parameters	19
4. SSC Gain States and Latitude Switching Points for December 1979, Descending Passes in the Northern Hemisphere	22
5. Relationship Between SSE and Gain for OLS Visible Data	25
6. Conversion of OLS IR Greyscale to Equivalent Blackbody Temperatures	27
7. DMSP F4 Orbital Parameters	28
8. Visible and SSC Greyscale and Corresponding Reflectivities Following Normalization by AFGL	30
9. Clear and Cloudy Categories	35

## Tables

10. AFGWC Test of Decision Matrix Given in Figure 22	55
11. Average Statistics	64
12. Results of Classifier Using Visible and IR Data	70
13. Ratios of SSC/Visible for Clear and Cloudy Categories	71
14. Results of Classifier Using Ratios of SSC/Visible Data	72
15. Results of Classifier Using SSC, Visible, and IR Data and Adapted From Hunt et al <sup>14</sup>	74
16. Results of Classifier Using SSC, Visible, and IR Data and Adapted From Kimball <sup>23</sup>	75
17. Results of Classifier Using the Woronicz Decision Matrix Modified to Separate Matrices for Land and Water Backgrounds	77
18. Comparison of Classification Accuracies for Woronicz Style SSC-Visible Decision Matrices	78
19. Results of Minimum Distance Classifier Using Unnormalized Means of SSC, Visible, and IR Data (Equation (7))	79
20. Results of Minimum Distance Classifier Using Normalized Means of SSC, Visible, and IR Data (Equation (8))	79
21. Results of Minimum Distance Classifier Using Unnormalized Means and Standard Deviations of SSC, Visible, and IR Data (Equation (9))	80
22. The Same Classifier Used for Table 21 (Minimum Distance Using Unnormalized Means and Standard Deviations, Equation (9)) Except That Results are Given for all Nine Categories of Clear Surfaces and Clouds	81
23. Comparison of Classification Accuracies	83

# Improved Cloud Detection Utilizing Defense Meteorological Satellite Program Near Infrared Measurements

## 1. INTRODUCTION

A near IR sensor at  $1.6 \mu\text{m}$  was flown on DMSP vehicle F-4 and provided experimental data from June to December, 1979. The sensor is identified as Special Sensor C (SSC) or as the snow-cloud discriminator. [The primary objective of the experiment was to discriminate snow cover from cloud cover and, in so doing, to improve the analysis of clouds on a world-wide basis.] This objective had been suggested by earlier studies<sup>1,2</sup> that found that snow covers were very poor reflectors of sunlight at  $1.6 \mu\text{m}$  while clouds were relatively good reflectors. An evaluation<sup>3</sup> of snow-cloud discrimination using SSC data has been made by the Air Force Global Weather Central (AFGWC).

[A secondary objective of the experiment was to distinguish water clouds from ice clouds since earlier studies also found that water clouds were good reflectors of sunlight at  $1.6 \mu\text{m}$  and appeared distinctly brighter than ice clouds.] Detecting water clouds would be a new and highly useful addition to satellite cloud analysis

---

(Received for publication 19 January 1982)

1. Valovcin, F. R. (1976) Snow/Cloud Discrimination, AFGL-TR-76-0174, ADA 032385.
2. Valovcin, F. R. (1978) Spectral Radiance of Snow and Clouds in the Near Infrared Spectral Region, AFGL-TR-78-0289, ADA 063761.
3. Woronicz, R. C. (1981) Results of AFGWC Snow Cloud Discrimination Study, AFGWC Technical Note 81-003.

since water clouds are the most opaque clouds for optical and infrared sensors on aircraft, weapons, and spacecraft. The water clouds tend to occur at low altitudes where they interfere with important Air Force operations such as the delivery of Precision Guided Munitions (PGM's). Finally, some liquid clouds are supercooled and may deposit ice on aircraft or cruise missiles passing through them.

Studies by Valovcin<sup>1,2</sup> and others have clearly demonstrated the potential for a satellite channel at 1.6  $\mu\text{m}$  to discriminate clouds from snow and water clouds from ice clouds. Data from the SSC allow a realistic evaluation of the potential improvements to cloud analysis at AFGWC. The SSC data were colocated with broadband visible (0.4 to 1.0  $\mu\text{m}$ ) and thermal IR (10.2 to 12.8  $\mu\text{m}$ ) from the Operational Linescan System (OLS) on the DMSP. Therefore, the extra cloud information offered by the SSC can be compared to the information already available from the OLS channels. Moreover, the polar-orbiting DMSP satellite carried the SSC over a variety of cloud types and backgrounds not observed in previous studies so that cloud decision parameters can be tested over global extremes to determine the best algorithm for future applications.

Studies to distinguish water clouds, ice clouds, and clear areas using SSC and OLS data are described in this report. The physical basis for discriminating water clouds and ice clouds in the near IR is discussed in Section 2 along with a summary of related reports. In Section 3, DMSP sensors are described along with examples of visible, near IR, and IR data. In Sections 4 and 5, algorithms for distinguishing cloud phase and cloud types are described and the results of classifications are given in Section 6. Options for improved analysis and suggestions for incorporating the decisions into the AFGWC Automated Cloud Analysis (3DNEPH) are given in Sections 7 and 8.

## 2. NEAR IR PROPERTIES OF CLOUDS

The ability of SSC measurements to distinguish water clouds from ice clouds is a result of the differing optical properties of water vapor, water droplets, and ice particles. The differing optical properties have a straightforward explanation in terms of molecular physics. According to a review by Hunt et al,<sup>4</sup> water molecules have active fundamental vibrational modes and overtones of modes, some of which absorb energy in the near IR. These vibrational modes exist for all phases of water but their peak absorption shifts to longer wavelengths as water vapor condenses to the liquid phase and also as liquid freezes to ice. The shift in wavelength

---

4. Hunt, G.R., Salisbury, J.W., and Bunting, J.T. (1974) Distinction Between Snow and Cloud in DMSP Satellite Imagery, Report to the Fourth AFCRL/AWS Satellite Working Group, 15 pp.

of the vibrational absorption bands is due to significant increases in intermolecular forces as the water molecules become more highly organized in the liquid and solid states. The near IR absorption properties of vapor, water, and ice summarized by Blau et al<sup>5</sup> and by Irvine and Pollack<sup>6</sup> indicate one peak in absorption centered near 1.38  $\mu\text{m}$  for water vapor, which shifts to about 1.45  $\mu\text{m}$  for liquid water, and 1.52  $\mu\text{m}$  for ice in laboratory measurements of pure water and ice.

The SSC channel is sensitive to energy at 1.51 to 1.63  $\mu\text{m}$ . This spectral region is sufficiently removed from the water vapor absorption band at 1.38  $\mu\text{m}$  to be an atmospheric window with minimal attenuation from sea level to the satellite. Figure 1 from Selby and McClatchey<sup>7</sup> has atmospheric transmittance from sea level to space with the bandwidth superimposed. The transmittance for the SSC channel is higher than the OLS visible and higher for most atmospheres than the OLS IR channel. At longer wavelengths, the SSC atmospheric window is bounded by another vibrational absorption band of water vapor which is centered at 1.87  $\mu\text{m}$ . Within the spectral region from 1.50 to 1.75  $\mu\text{m}$  ice absorption exceeds liquid water absorption significantly according to Table 1 derived from Irvine and Pollack.<sup>6</sup> If  $I_0$  is the intensity of radiation incident on a cell containing ice or water,  $I$  is the intensity transmitted through thickness  $X$ , and  $R$  the fraction of the incident light that is reflected, then the absorption coefficient  $k$  in Table 1 can be determined from

$$I = (1 - R) I_0 \exp(-kX) \quad (1)$$

The increased absorption by ice is due in part to the shift of the absorption band to higher wavelengths from liquid to solid states and also in part to the fact that the absorption band for ice is generally stronger than the band for water.

A similar set of displacements in absorption bands exists for wavelengths greater than 1.87  $\mu\text{m}$ , the center of another absorption band for water vapor. These result in another window near 2.1  $\mu\text{m}$  in which water clouds are observed to differ from ice clouds. This window has been studied<sup>4, 8, 9</sup> but does not appear

5. Blau, H.H., Jr., Espinola, R.P., and Reifenstein, E.C., III (1966) Near infrared scattering by sunlit terrestrial clouds, Applied Optics 5(No. 4): 555-564.
6. Irvine, W.M., and Pollack, J.B. (1968) Infrared optical properties of water and ice spheres, Icarus 8:324-360.
7. Selby, J.E.A., and McClatchey, R.A. (1975) Atmospheric Transmittance From 0.25 to 28.5  $\mu\text{m}$ : Computer Code Lowtran 3, AFCRL-TR-75-0255, ADA 017734.
8. Blau, H.H., Jr., and Hovis, W.A. (1971) Cloud characteristics from infrared measurements, Space Research XI, Akademie-Verlog, Berlin, pp. 731-739.
9. Alishouse, J.C., Jacobowitz, H., and Wark, D.Q. (1976) A Cloud Physics Investigation Utilizing Skylab Data, Final Report to Johnson Space Center, Houston, Texas.

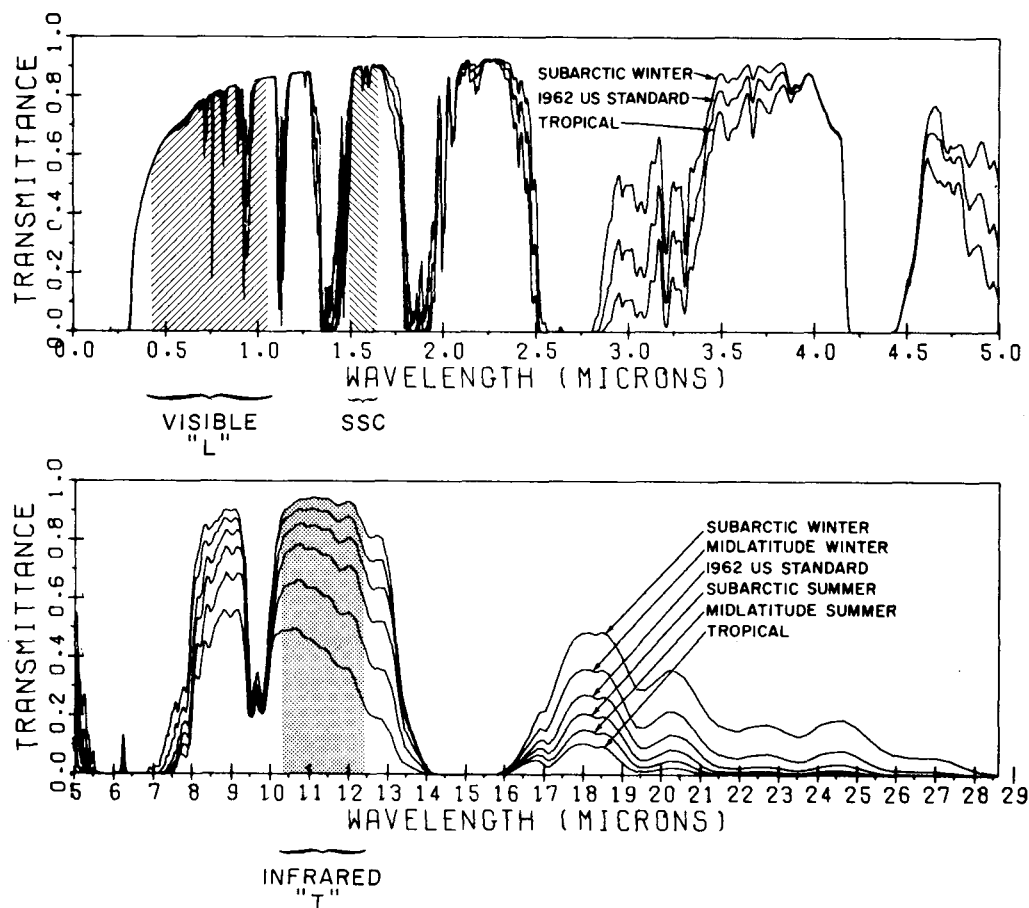


Figure 1. Atmospheric Transmittance for a Vertical Path to Space From Sea Level for Six Model Atmospheres. The bandwidths of 50 percent response are indicated for the SSC and OLS visible and IR channel

Table 1. Absorption Coefficient for Ice and Water vs Wavelength

Wavelength ( $\mu\text{m}$ )	Wavenumber ( $\text{cm}^{-1}$ )	$k$ ( $\text{cm}^{-1}$ ) Ice	$k$ ( $\text{cm}^{-1}$ ) Water
1.50	6667	46.8	17.3
1.55	6452	47.4	9.6
1.60	6250	29.9	6.2
1.65	6061	23.1	5.1
1.70	5882	14.2	5.2
1.75	5714	10.2	6.4

to be as sensitive as the 1.6  $\mu\text{m}$  window for discriminating water clouds from ice clouds.

Spectral measurements of water and ice clouds are highly consistent with the laboratory measurements of water and ice. An example of recent measurements by aircraft is given in Figure 2 taken from Valovcin.<sup>2</sup> These measurements were taken by an interferometer onboard the AFGL KC-135 aircraft. The interferometer provided spectral signatures of cumulus and cirrus clouds and also of snow cover. These spectra represent solar energy backscattered from clouds or snow so that they are inversely related to the absorption properties of the clouds or snow. Low numbers in Figure 2 represent weak scattering, which implies strong absorption. Cumulus clouds were observed to be good reflectors, cirrus clouds were weak reflectors, and snow covers were poor reflectors. These observations agree with studies using aircraft<sup>8,10</sup> and Skylab satellite<sup>9,11</sup> observations, which also support satellite discrimination of water clouds from ice clouds and clouds from snow using measurements at 1.6  $\mu\text{m}$ .

The reflectivities of clouds can also be calculated using radiative transfer models. These models assume that the complex index of refraction is known for the wavelength of radiation and phase of water considered and that clouds can be adequately represented by a size distribution of particles having some simple shape, such as a sphere or cylinder. Some other necessary assumptions are the shape of the cloud, which is usually an infinite slab but sometimes a cube or a cylinder, and its thickness.

For water clouds, the calculations are generally considered to be in agreement with observed reflectivities despite the fact that it is difficult if not impossible to measure accurately all of the cloud parameters mentioned within the field of view of a satellite. An aircraft can sample only parts of a cloud and particle sizes are often observed to vary within the clouds. However, both calculations and observations show that water clouds are good reflectors near 1.6  $\mu\text{m}$ <sup>8,10</sup> and tend to appear much as they do in broadband visible channels.

For ice clouds, reflectivities are calculated with much less confidence. Within the strongly-illuminated upper region of one ice cloud, an aircraft may encounter particles classified as prisms, plates, dendrites, and smaller fragments with

- 
10. Kyle, H.L., Curran, R.J., Barnes, W.L., and Escoe, D. (1978) A Cloud Physics Radiometer, Proceedings of the 3rd Conf. on Atmospheric Radiation, Davis, California, p. 107.
  11. Barnes, J.C., Smallwood, M.D., and Cogan, J.L. (1975) Study to Develop Improved Spacecraft Snow Survey Methods Using Skylab/EREP Data, ERT Document No. 0412-F, Final Report, Contract No. NAS9-13305, Environmental Research & Technology Inc., Concord, Massachusetts, 92 pp.

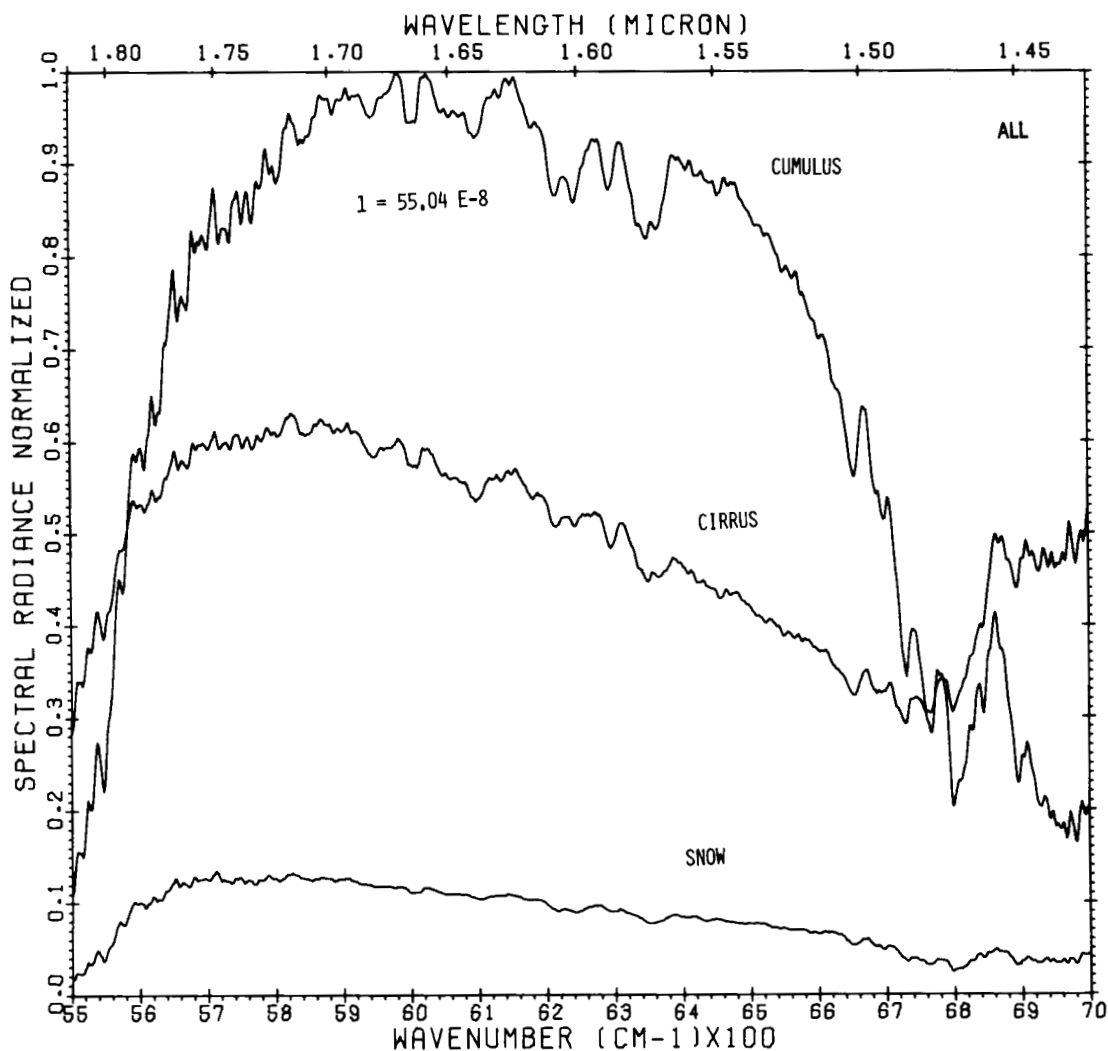


Figure 2. Average Spectral Radiance for 36 Cases of Cumulus, 32 Cases of Cirrus, and 56 Cases of Snow from Valovcin.<sup>2</sup> The plots are normalized such that the maximum radiance of  $55.04 \times 10^{-8} \text{ W cm}^{-2} \text{ sr}^{-1} (\text{cm}^{-1})^{-1}$  has a value of 1.0

dimensions varying from 10 to over  $1000 \mu\text{m}$ .<sup>12</sup> The classifications are often difficult to make since most ice particles are irregular in shape. Optical effects that are not modeled in calculations using spheres to approximate the ice particles, such as specular reflections from flat particles, have been observed.<sup>12</sup>

An example of calculations for both water and ice clouds is given in Figure 3, which is reproduced from Blau and Hovis.<sup>8</sup> Relative reflectance between water and

12. Bunting, J. T. (1980) Sensing Ice Clouds From Satellites, Light Scattering by Irregularly Shaped Particles, (D. W. Schuerman, ed.) Plenum Press, New York, p. 25.

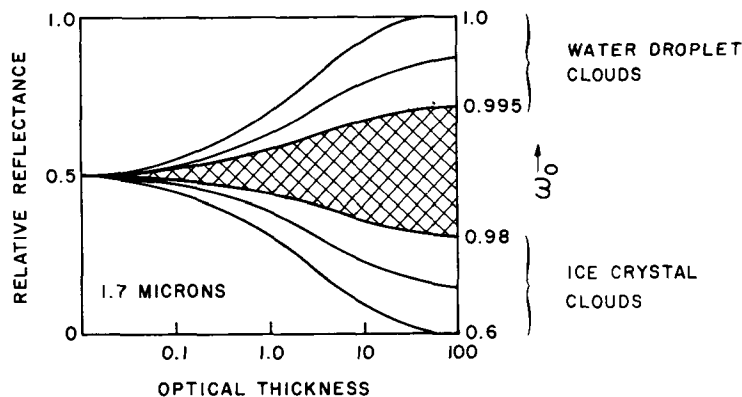


Figure 3. Calculated Cloud Reflectance as a Function of Optical Thickness and Single Scattering Albedo According to Blau and Hovis<sup>8</sup>

ice clouds is presented as a function of optical thickness and single-scatter albedo,  $\omega_0$ . Water clouds had single-scatter albedoes from 1.0 to 0.995 based on Mie calculations for spheres of radius between 2 and 30  $\mu\text{m}$ . Ice clouds had single-scatter albedoes from 0.98 to 0.6 for spheres of radius between 25 and several hundred micrometers. A relative reflectance of 0.5 was used at zero optical thickness to represent a bare land background, which is expected to be more reflective at 1.7  $\mu\text{m}$  than at visible wavelengths.

Where the optical thickness is large in Figure 3, there is a good separation of water clouds and ice clouds by reflectivity. For a given optical thickness, the relative reflectivities decrease as the single-scatter albedo decreases. The single-scatter albedo,  $\omega_0$ , can be defined as the ratio of energy scattered to the sum of energy scattered and absorbed per particle. For a given particle size,  $\omega_0$  decreases as the absorption coefficient of the particle material increases such as from water to ice at 1.7  $\mu\text{m}$ . For a given material,  $\omega_0$  tends to decrease as the particle size increases, since scattering is less efficient. Therefore, ice clouds have significantly lower single-scatter albedos at this wavelength since ice absorbs more than water and since the ice particles are much larger than water droplets. Cloud reflectivity decreases as the single-scatter albedo decreases since sensors receive less energy from single and multiple scatterings.

More recent and extensive calculations by Twomey and Seton<sup>13</sup> have supported the conclusion that the reflectivity of water clouds decreases as the droplet size increases. They also show how the cloud optical thickness, single-scatter albedo,

13. Twomey, S., and Seton, K.J. (1980) Inferences of clouds from spectral reflectance measurements, *J. Atmos. Sci.* 37:1065-1069.

and asymmetry factor can be scaled and interrelated for improved inference of the gross microphysical properties of clouds from near IR reflectance measurements.

The concept of decreasing reflectivity with increasing particle size can be extrapolated. In the absence of specular reflection or foamy conditions, open water surfaces such as oceans appear to be very poor reflectors at visible and near IR frequencies as examples in the next sections will demonstrate. The explanation is that viewing the ocean is equivalent to looking at a water drop with a radius of the earth. The fact that the oceans do not extend to the center of the earth does not make a difference to the scattering or reflection properties since the oceans are deep enough to absorb all sunlight which is not reflected at the surface or by particles suspended in the water. The oceans are observed to be the poorest reflectors in comparison to the much smaller particles of water clouds, ice clouds, or snow cover. This line of reasoning is only valid for viewing angles and wavelengths of radiation for which a water surface is a poor reflector and would not work for the viewing geometry of specular reflection, grazing incidence, or at microwave frequencies where oceans are good reflectors.

Figure 3 shows that the total reflectance of an ice cloud over a land background varies from 0.5 to 0 as the optical thickness increases and  $\omega_0$  decreases. A broad range of optical thicknesses are observed for ice clouds as is evident from the cloud mass and snow cover mass estimates in Table 2.<sup>14, 15</sup> The thinnest clouds, sometimes called "invisible cirrus", would appear nearly the same as cloud-free backgrounds while thicker ice clouds could be confused with darker scenes. Water clouds, on the other hand, are less likely to be optically thin due to higher cloud mass and smaller particle size so they are expected to be better reflectors than most backgrounds.

Since their scattering properties are similar, ice clouds could be confused with snow covers. However, observations by Valovcin<sup>2</sup> and Barnes et al<sup>11</sup> show that snow cover tends to appear darker than ice clouds at 1.6  $\mu\text{m}$ . The coldest ice cloud particles<sup>12</sup> are smaller than snow particles and are expected to scatter more light at 1.6  $\mu\text{m}$ . Table 2 indicates that snow covers will tend to have a greater total mass of ice to absorb sunlight at 1.6  $\mu\text{m}$ . The highest total mass of ice cloud observed by AFGL cloud physics aircraft and radars<sup>16</sup> is 0.42 g/cm<sup>2</sup> observed over Kwajalein Atoll. Ice particles existed from cloud tops at 15.5 km down to the bottom of the melting layer at 4.3 km. Dividing the total mass by 0.917 g/cm<sup>3</sup>, an

14. Wiscombe, W. J., and Warren, S. G. (1981) A model for the spectral albedo of snow, J. Atmos. Sci. 37:2712-2733.
15. Conover, J. H., and Bunting, J. T. (1977) Estimates From Satellites of Weather Erosion Parameters for Reentry Systems, AFGL-TR-77-0260, ADA 053654.
16. Plank, V. G. (1978) Weather Documentation for ANT-II, Launched 4 July 1978, AFGL 60 Day Report.

Table 2. Properties of Water Clouds, Ice Clouds, and Snow Cover

	Particle Radius ( $\mu\text{m}$ )		Mass of Water or Ice ( $\text{g}/\text{m}^2$ )	
	Min	Max	Min	Max
Water Cloud	2	30	$10^1$	$10^4$
Ice Cloud	25	300	$10^{-1}$	$10^4$
Snow Cover	50	200	$10^3$	$10^6$

The particle sizes for water and ice clouds are for the spheres used by Blau and Hovis<sup>8</sup> in their calculations. The particle sizes for snow cover are for spheres used by Wiscombe and Warren.<sup>14</sup> The mass estimates for water and ice clouds were based on a measurement program described by Conover and Bunting.<sup>15</sup> The mass estimates for snow cover correspond to snow depths from 1 cm to 10 m

average density for ice from Hobbs,<sup>17</sup> gives an equivalent depth of 0.46 cm of solid ice. Using a 10 to 1 ratio of snow depth to water content, this figure is equivalent to a snow cover of only 4.6 cm. The highest observation of total ice over temperate latitudes was  $0.31 \text{ g}/\text{cm}^2$  which is equivalent to 3.4 cm of snowfall. These depths of 4.6 or 3.4 cm would be thin snow covers. Higher snowfalls are common since the snowfall takes place over considerable time and the amount of snow accumulation in one hour is on the order of the total vertical ice content at a particular time. This approximation can be derived from fallspeeds of snowflakes<sup>17</sup> and characteristic depths of snow clouds.

Although the difference in total absorbing mass between snow cover and ice clouds may be sufficient to explain why snow appears darker than ice clouds at  $1.6 \mu\text{m}$ , it is also true that snow crystals will change size and shape with time and these changes may decrease the reflectivity of snow cover. Hobbs<sup>17</sup> describes how dry snowflakes may become increasingly rounded in shape and eventually break up into smaller grains which are fairly uniform in size. O'Brien and Munis<sup>18</sup> have noted that melting and refreezing of snow cover tends to decrease reflectance at 1.2 to  $1.9 \mu\text{m}$ . In summary, the density of both dry and wet snow covers tends to increase with time but the reflectivity at  $1.6 \mu\text{m}$  remains rather low.

Many land scenes are moderately reflective and could be confused with clouds at  $1.6 \mu\text{m}$ . According to Goetz and Rowan,<sup>19</sup> the region around  $1.6 \mu\text{m}$  exhibits

17. Hobbs, P.V. (1974) *Ice Physics*, Clarendon Press, Oxford.
18. O'Brien, H.W., and Munis, R.H. (1975) *Red and Near Infrared Spectral Reflectance of Snow*, ERP No. 332, U.S. Army Cold Regions and Engineering Laboratory, Hanover, New Hampshire.
19. Goetz, A.F.H., and Rowan, L.C. (1981) *Geologic remote sensing*, Science 211(No. 4484):781-791.

the highest reflectance for most rocks because it is nearly midway between the ultraviolet-visible iron absorption bands and a strong fundamental OH<sup>-</sup> vibration at 2.74  $\mu\text{m}$ . Field-acquired reflectance spectra often exceed 50 percent for rocks free of vegetation. Altered rocks containing clay may exhibit reflectance greater than 70 percent.<sup>20</sup> Vegetation often has a lower reflectance than rocks and Goetz and Rowan<sup>19</sup> show reflectances less than 20 percent for Ponderosa pine. However, certain moist leaves have been found by laboratory measurements<sup>21</sup> to have a reflectance over 50 percent. Reflectances in the range of 50 to 70 percent are expected to be higher than those observed for ice clouds and as high as some water clouds. In fact, aircraft measurements<sup>22</sup> at 1.6  $\mu\text{m}$  over farmland and deserts were found to be as bright as some water clouds although most water clouds were brighter.

In general, there has been interest in the near IR windows from a variety of disciplines and the literature on applications is growing rapidly. Cloudfree land is expected to have 1.6  $\mu\text{m}$  reflectivity varying with changes in vegetation, exposed rocks, and soil. Ice clouds have reflectivities reasonably close to and sometimes lower than cloudfree land so that detecting ice clouds over land requires extra information such as the OLS channels in different spectral regions.

### 3. DMSP IMAGERY DATA

#### 3.1 Special Sensor C

According to descriptions<sup>23</sup> by the manufacturer, Westinghouse Electric Corporation (WEC), the SSC sensor is a staring radiometer with an array of 48 detector elements in the image plane. Image data are generated by a "push-broom" type of scan. The total view of the 48 detector elements can be likened to a 401 nmi wide broom across the track of the 5D spacecraft that is pushed along the track by the spacecraft orbital velocity. The sensor was mounted 20° off the nadir angle so that an edge of its field of view (FOV) is at nadir while the other edge intersects the earth at a distance of 401 nmi from the nadir. An example of data coverage for

- 
20. Rowan, L. C., Goetz, A. F. H., and Ashley, R. P. (1977) Geophysics 42:522.
  21. Anderson, A. G. (1976) Resource and Environmental Surveys From Space With The Thematic Mapper in the 1980's, Report of the National Research Council Committee on Remote Sensing Programs.
  22. Nelgner, H. D., and Thompson, J. R. (1962) Airborne Spectral Radiance Measurements of Terrain and Clouds, Emerson Electric of Saint Louis, Report No. 1323 (RPA 6-62).
  23. Kimball, A. W. (1980) Technical Operating Report, SSC Data Evaluation, Westinghouse Electric Corporation, Defense and Electronic Systems Center, Baltimore, Maryland.

orbit 2680 (12 December 1979) between latitudes 80°N and 20°N is shown in Figure 4. The width of SSC data scans is indicated as a narrow-shaded swath while the edges of scans by the OLS visible and IR imager are shown as lines parallel to the spacecraft subtrack and over 800 nmi from it. DMSP vehicle F4 is descending over the eastern coast of North America at about local noon. The SSC data lies to the east of the spacecraft subtrack.

The SSC lens arrangement is a 5-element unit with distortions controlled such that all of the 48 detector channels have an Instantaneous FOV (IFOV) of 14.6 mrad along track and 9.1 mrad cross track. The spacing of channels is 14.6 mrad across track so that scan spots are not contiguous along the direction of scan. The major system parameters of the SSC are summarized in Table 3.

Table 3. SSC Major System Parameters

Item	Value	Units
Number of Channels	48	--
Spectral Band	1.51 to 1.63	μm
Output Data Quantization	6	Bits
Data Frame Time	2	sec
Output Data Burst Rate	1	kHz
Each Channel Time Constant	0.68	sec
Multiplex Time per Channel	10	msec
Chopper Modulating Frequency	77	Hz
IFOV Each Channel	14.6 × 9.1	mrad

Figure 5 has approximate footprints of SSC and OLS on the earth's surface for selected SSC channels from 1 to 48. The SSC footprints are IFOV's projected on the earth. The actual measurements are very slightly smeared in the along-track direction since sampling a channel takes 0.01 sec and the spacecraft is moving. The alignment of SSC scan spots is not exactly perpendicular to the spacecraft track since the spacecraft advances about 1.7 nmi during the 0.48 sec total sampling time for one line of 48 spots.

The SSC provided 6-bit data quantization, which allows images with 64 grey-shades. A series of gain settings were used while operating the SSC to minimize the great variation of solar illumination as the spacecraft enters daylight at the

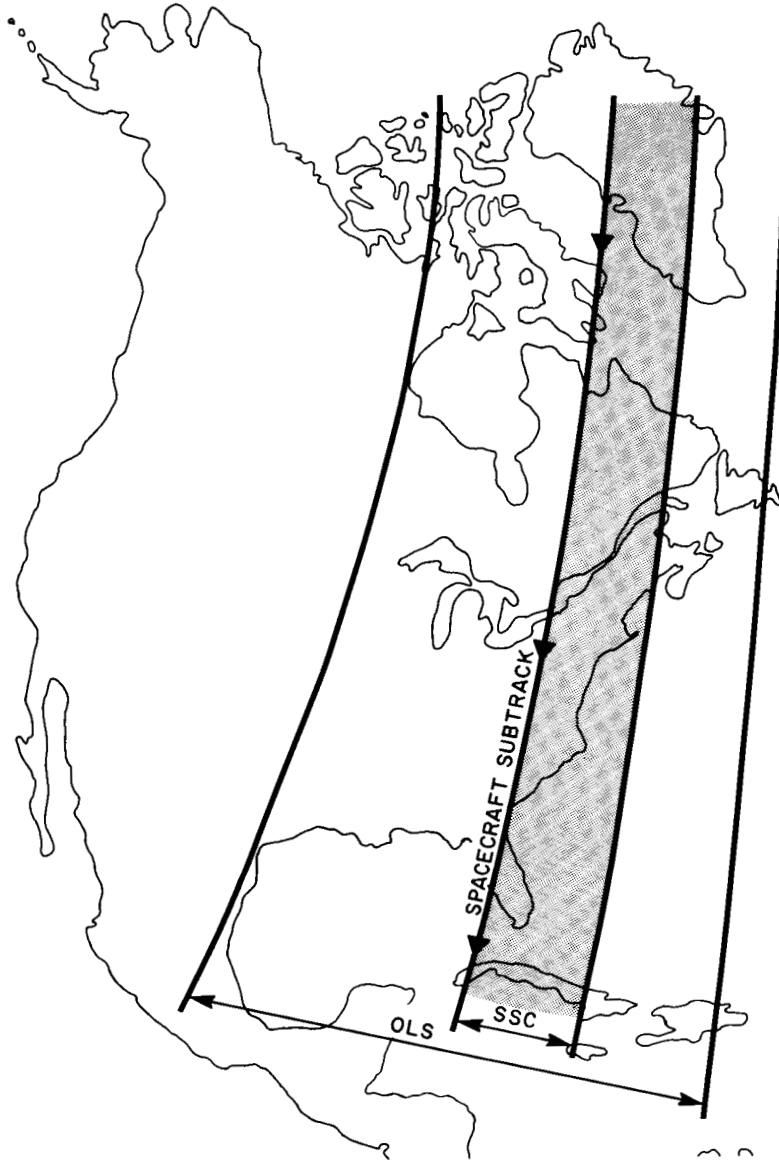


Figure 4. The Horizontal Extent of Data Provided by OLS and SSC Sensors in a Partial Orbit

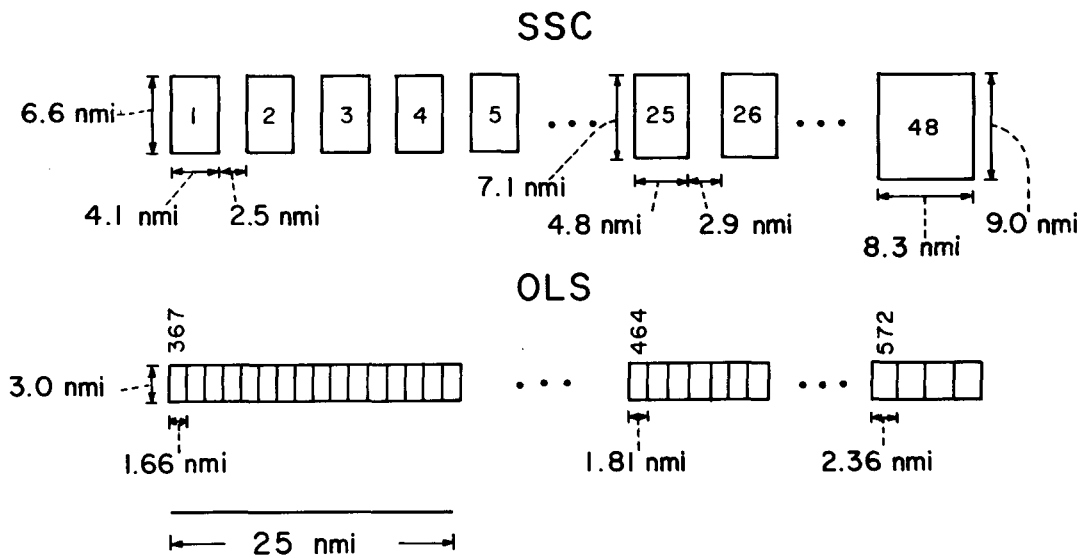


Figure 5. Approximate Ground Resolution of SSC and OLS Data. SSC channel numbers are given inside each box. Channel 1 is on the subtrack

terminator and descends to maximum illumination near the equator. Table 4 has the available gain states along with the latitude switching points for the Northern Hemisphere during December 1979. During the first few months of operation of the SSC, the AFGWC<sup>3</sup> and WEC experimented with gain settings and decided to use relatively low gain settings so that the sensor would saturate as little as possible.

The SSC was calibrated using the Visible Uniform Light Source at the WEC. Channel 24 was used for calibration adjustments. For the bandwidth of the SSC, the solar energy from a perfectly diffuse reflector was estimated to be  $9.92 \times 10^{-4} \text{ W/cm}^2/\text{sr}$ . During calibration, full-scale output at gain state zero was found to be  $5.06 \times 10^{-4} \text{ W/cm}^2/\text{sr}$ , which implies SSC saturation at 51 percent of the incident solar radiation at the top of the atmosphere when the sun is overhead.

Table 4. SSC Gain States and Latitude Switching Points for December 1979, Descending Passes in the Northern Hemisphere

State	Word	dB	Gain Ratio	Switching Latitude
15	1 1 1 1	36.0	63.10	Not used
14	1 1 1 0	33.6	47.86	Not used
13	1 1 0 1	31.2	36.31	Used above 69.63 N
12	1 1 0 0	28.8	27.54	69.63 N
11	1 0 1 1	26.4	20.89	69.11 N
10	1 0 1 0	24.0	15.85	68.41 N
9	1 0 0 1	21.6	12.02	67.49 N
8	1 0 0 0	19.2	9.12	66.26 N
7	0 1 1 1	16.8	6.92	64.62 N
6	0 1 1 0	14.4	5.25	62.44 N
5	0 1 0 1	12.0	3.98	59.51 N
4	0 1 0 0	9.6	3.02	55.56 N
3	0 0 1 1	7.2	2.29	50.19 N
2	0 0 1 0	4.8	1.74	42.69 N
1	0 0 0 1	2.4	1.32	31.74 N
0	0 0 0 0	0.0	1.00	13.17 N

Switching occurs when the satellite subtrack crosses the switching latitude.  
 $\text{dB} = 20 \log (\text{gain ratio})$ .

Later calculations that used the actual operating temperature of the SSC in the spacecraft suggested that saturation would occur at 53 percent.

When the sun is not overhead, higher reflectivities can be observed by using appropriate gain settings. In fact, most of the gain settings given in Table 4 cause the sensor to saturate over scenes of about 60 percent reflectivity. Some of the most reflective scenes for the SSC spectral band, which were generally water clouds, would still saturate the sensor at 60 percent reflectivity.

### 3.2 OLS IR and Visible

The OLS is the primary sensor on DMSP spacecraft. The OLS is a dual channel scanning radiometer that senses reflected light and emitted infrared energy in the 0.4 to 1.0  $\mu\text{m}$  and 10.2 to 12.8  $\mu\text{m}$  spectral bands, respectively. The reflected light is called L or visible data while the infrared energy is called T or IR data. Both visible and IR energy are captured by a scanning telescope system with optics driven across the spacecraft subtrack in a sinusoidal motion by counter-reacting coiled springs. The incoming beam of energy is split into two separate paths and then focused onto separate visible and IR detector elements. The sinusoidal scanning moves the IFOV of these elements across the subtrack with maximum scanning velocity when looking straight down (nadir) and reversals of velocity at the edges of scan. The change of scan velocity with scanning angle allows the spacing of measurements on the earth's surface to be nearly constant going from the subtrack toward the edge of scan. The detector sizes are reduced at high scan angles so that projected IFOV maintains near constant resolution on the earth's surface. The more advanced design of the OLS enables the earth sampling to change much less as scanning proceeds from nadir to higher scan angles. The improvement can be noted by comparing the left side of Figure 5 (nadir or subtrack) to the right side (401 nmi from nadir). The OLS data described in this report were smoothed twice: first, on the satellite from 0.3 nmi to 1.5 nmi, and then at GWC from 1.5 nmi to 3 nmi. In Figure 5, small rectangles represent the approximate sizes and locations of 3 nmi OLS data. These are not sensor footprints since each 3 nmi data value is in fact an average over 10 scan lines of OLS fine mode (0.3 nmi) visible or IR data. The along-track length is arbitrarily shown as 3.0 nmi even though it is slightly less near the subtrack. The cross-track spacing of these data values varies from 1.66 nmi at the subtrack (sample number 367) to 2.36 nmi at 401 nmi from subtrack (sample number 574).

These distances are computed by constructing a triangle with vertices at the satellite, the earth's center, and the satellite viewing point, and then applying simple trigonometric equations to compute the arc distances on the earth subtended by appropriate satellite viewing angles. The following equation relates sensor scan angle  $\phi$  to OLS sample number (left side of scan is negative):

$$\phi = \phi_p \cos \left[ \frac{(i-1)m}{N} + B \right] , \quad (2)$$

where  $\phi_p = 1.009673$  radians is the peak scan angle,  $i$  is the OLS sample number,  $N = 732.218$  is the nominal number of OLS samples,  $m = 2.6687426$  radians, and  $B = 0.2368551$  for visible data, 0.2359074 for IR data. ( $\phi$  is measured from satellite nadir.)

Also shown in Figure 5 is a line representing the distance 25 nmi, which is the spacing of the 3DNEPH<sup>24</sup> grid at 60° latitude. An 8 × 8 array of gridded 3 nmi data are analyzed for cloud cover in the 3DNEPH after the data are mapped onto a polar stereographic projection. Applications of SSC and OLS data averaged to 25 nmi resolution are described in the next section.

On the spacecraft, visible data are digitized into one of 128 possible greyscale values (that is, 7 bits). At AFGWC,<sup>3</sup> these greyscales are truncated to 64 possible values (6 bits). A sensitive procedure has been developed for controlling the gain of OLS visible sensing on the spacecraft. The gain is automatically controlled by the value of SSE (Scene Solar Elevation or solar elevation at the viewed point on the earth) calculated by the spacecraft. The relation between gain and SSE is given in Table 5. Non-integer values are interpolated and granularity is 0.125 dB. The spacecraft knows  $\phi$ , the scan angle of the OLS. The geocentric angle  $\Theta$  of the scene from the spacecraft subpoint is given by:

$$\Theta = \sin^{-1} \left( \frac{R_e + h}{R_e} \sin \phi \right) - \phi , \quad (3)$$

where  $R_e$  is the earth radius and  $h$  is the spacecraft altitude. Given solar elevation  $E$  and azimuth  $A$  at the spacecraft,

$$\text{SSE} = E + \Theta \cos A \quad (4)$$

to a good approximation and SSE controls the gain. The gain changes are smooth enough so that they were never noticed in the 3 nmi data. On the other hand, the SSC gain changes were quite noticeable at low solar elevations due to the much greater granularity of the SSC gain changes and the fact that when the gain changed all 48 SSC detectors would change and appear as a linear discontinuity in the data swath.

The OLS visible channel was calibrated to a full-scale output at gain state zero of  $2.12 \times 10^{-2}$  W/cm<sup>2</sup>/sr. Considering the inband solar energy, this value implies saturation at 80 percent of the incident solar radiation at the top of the atmosphere when the sun is overhead. Therefore, the OLS can discriminate more reflective scenes than the SSC, which tended to saturate at 60 percent reflectivity. In the course of this study, very few instances of saturated OLS visible measurements were observed and these were from cumulonimbus clouds at low latitudes.

Like the visible data, OLS IR data are digitized into one of 128 possible greyscale values on the satellite and are truncated to one of 64 possible values at

24. Fye, F.K. (1978) The AFGWC Automated Cloud Analysis Model, AFGWC Technical Memorandum 78-002.

Table 5. Relationship Between SSE and Gain for OLS Visible Data

SSE, Degrees	GAIN, dB	SSE, Degrees	GAIN, dB
0	33.33	45	2.37
1	27.35	46	2.26
2	22.49	47	2.15
3	18.72	48	2.05
4	15.94	49	1.94
5	14.00	50	1.84
6	12.70	51	1.74
7	11.86	52	1.64
8	11.31	53	1.55
9	10.90	54	1.46
10	10.53	55	1.37
11	10.16	56	1.28
12	9.76	57	1.20
13	9.35	58	1.12
14	8.93	59	1.04
15	8.53	60	0.97
16	8.16	61	0.91
17	7.83	62	0.85
18	7.53	63	0.79
19	7.24	64	0.73
20	6.97	65	0.68
21	6.70	66	0.63
22	6.43	67	0.57
23	6.16	68	0.52
24	5.90	69	0.48
25	5.64	70	0.43
26	5.40	71	0.39
27	5.17	72	0.36
28	4.96	73	0.32
29	4.76	74	0.29
30	4.57	75	0.25
31	4.39	76	0.22
32	4.22	77	0.19
33	4.05	78	0.15
34	3.89	79	0.12
35	3.73	80	0.10
36	3.58	81	0.08
37	3.43	82	0.06
38	3.28	83	0.05
39	3.14	84	0.04
40	3.00	85	0.03
41	2.87	86	0.02
42	2.74	87	0.02
43	2.61	88	0.01
44	2.49	89	0.00
		90	0.00

dB = 20 log (Gain Ratio). The Gain Ratio is the factor of increase relative to an overhead sun, for which SSE = 90 degrees

AFGWC. The IR detectors are designed to produce an output signal strength directly proportional to the equivalent blackbody temperature within the sensor FOV. The maximum temperature detectable is 310°K and the minimum is 210°K (Table 6). The warmer scenes tend to have considerable atmospheric attenuation so that the equivalent blackbody temperatures are less than the true scene temperature. The AFGWC determines corrections to convert the apparent temperature to surface temperature for clear conditions.<sup>3</sup> The corrections vary from 15° at 310°K down to 1° at 210°K. Transmission models have also been used to calculate temperature corrections as a function of the amount of water vapor in the column of air between the satellite and the surface.<sup>25</sup> The results can be used to estimate cloud top temperatures.

### 3.3 Earth Location, Colocation, and Normalization

The ability to earth-locate, colocate, and normalize SSC and OLS data was required before the sensors could be compared and the extra information provided by the SSC could be determined. Earth-location, colocation, and normalization of SSC and OLS data were done using the AFGL Man-computer Interactive Data Access System (McIDAS) before image analysis and algorithm development were done.

Earth-location is an automated procedure to determine the latitude and longitude of every data element given the time of a scan line and the scanning angle. Earth-location is particularly valuable for cloudy or partly cloudy scenes when landmarks are not visible. It is particularly valuable to the image analyst since it allows non-satellite information on vegetation, exposed rocks and soils, snow cover, and surface weather data to be compared to the satellite data.

Earth-location software was developed for the McIDAS for both SSC and OLS data. The software enabled the McIDAS operator to call for the geographical coordinates of any satellite data displayed on the TV screen. These coordinates would be calculated and displayed in less than one second. The equations we used to calculate the geographical coordinates of a DMSPP datum (also known as picture element or pixel) are presented in detail in a technical report by Ruff and Gruber<sup>26</sup> and will not be repeated here. They assume a spherical earth, a circular satellite orbit, a scan-line perpendicular to the satellite subtrack, and the time and location of ascending nodes for individual orbits. None of the above assumptions are true, but the errors in calculated locations were found to be minimal by checking clear landmarks such as islands and coastlines. Table 7 has the orbital parameters for

25. Fett, R. W., and Bohan, W. A. (1980) Navy Tactical Application Guide, Volume 3, NAVENVPREDRSCHFAC Technical Report 80-07 (pp. 1A20 to 1A22).
26. Ruff, I., and Gruber, A. (1975) Graphical Relations Between a Satellite and a Point Viewed Perpendicular to the Satellite Velocity Vector (Side Scan), NOAA Technical Memorandum NESS 65.

Table 6. Conversion of OLS IR Greyscale to Equivalent Blackbody Temperatures\*

Greyscale	IR Temperature		Greyscale	IR Temperature	
	K(deg)	C(deg)		K(deg)	C(deg)
0	310.0	37.0	32	259.2	-13.8
1	308.4	35.4	33	257.6	-15.4
2	306.8	33.8	34	256.0	-17.0
3	305.2	32.2	35	254.4	-18.6
4	303.7	30.7	36	252.8	-20.2
5	302.1	29.1	37	251.2	-21.8
6	300.5	27.5	38	249.7	-23.3
7	298.9	25.9	39	248.1	-24.9
8	297.3	24.3	40	246.5	-26.5
9	295.7	22.7	41	244.9	-28.1
10	294.1	21.1	42	243.3	-29.7
11	292.5	19.5	43	241.7	-31.3
12	291.0	18.0	44	240.1	-32.9
13	289.4	16.4	45	238.5	-34.5
14	287.8	14.8	46	237.0	-36.0
15	286.2	13.2	47	235.4	-37.8
16	284.6	11.6	48	233.8	-39.2
17	283.0	10.0	49	232.2	-40.8
18	281.4	8.4	50	230.6	-42.4
19	279.8	6.8	51	229.0	-44.0
20	278.3	5.3	52	227.4	-45.6
21	276.7	3.7	53	225.8	-47.2
22	275.1	2.1	54	224.3	-48.7
23	273.5	0.5	55	222.7	-50.3
24	271.9	-1.1	56	221.1	-51.9
25	270.3	-2.7	57	219.5	-53.5
26	268.7	-4.3	58	217.9	-55.1
27	267.1	-5.9	59	216.3	-56.7
28	265.6	-7.4	60	214.7	-58.3
29	264.0	-9.0	61	213.1	-59.9
30	262.4	-10.6	62	211.6	-61.4
31	260.8	-12.2	63	210.0	-63.0

\*The conversion is linear.

Table 7. DMSP F4 Orbital Parameters

Orbit (Rev. No.)	Date MM, DD, YY	A. Node <sup>o</sup> W of Prime Meridian	Universal Time of AN (GMT) HH, MMSS
2652	12. 10. 79	261.3	15. 2811
2680	12. 12. 79	256.4	15. 0848
2893	12. 27. 79	259.6	15. 2148
2879	12. 26. 79	264.5	15. 4115
2765	12. 18. 79	252.7	14. 5358
2751	12. 17. 79	257.5	15. 1322
2737	12. 16. 79	262.4	15. 3241
2552	12. 03. 79	Not Available	
2623	12. 08. 79	250.3	14. 4427
Inclination: $98.76^{\circ} \pm 0.12^{\circ}$			
Orbital Period: 6088 sec $\pm 0.5$ sec			
Altitude (near nominal): 833 km			

DMSP vehicle F4, which had the SSC sensor onboard. The locations and times of ascending node for the orbits used in this study are also listed in Table 7. This information is needed for earth-location.

SSC data were colocated with OLS visible and IR data by AFGWC. Since the OLS data have a finer resolution than the SSC data, the OLS data were averaged to approximate the resolution of the SSC footprint. The OLS data had to be relocated as well since the OLS scans differently. The resulting set of visible, IR, and SSC imagery were extremely useful for both subjective analysis and the development of automated analysis. An example is shown in Figure 6, which is a McIDAS display of data over the Eastern U.S.A. The SSC data are in the middle of Figure 6, while the averaged and relocated OLS visible and IR are on the left and right, respectively. More examples appear in the next section of this report.

The AFGWC smoothed and relocated the 3 nmi OLS data using the times of the scan-lines and the angles of data elements along the lines. It was not necessary to earth-locate the data to colocate them. Although the spacecraft computer keeps time to a much higher accuracy, the SSC data from AFGWC had times to the nearest

second for each scan-line. This timing was adequate since each line of SSC measurements took two seconds.

Figure 5 shows that the SSC footprints are about 2 to 2.5 times as long as the OLS footprints in the along-track direction. Along the scan lines, the SSC footprints are about 2 times as wide as the OLS at element 1, on the subtrack, and about 3 times as wide at element 48. Therefore, the footprint of element 1 contains 4 OLS footprints while the footprint of element 48 contains 6 to 9 OLS footprints. At AFGL, we experimented with averaging and relocating 3 nmi OLS data into SSC footprints but we found we could not significantly improve the AFGWC approach.

We are aware of several reasons why the averaged OLS footprints are not identical to the SSC footprints. First of all, the SSC scan line times are only known to the nearest second. Moreover, the 3 nmi OLS data is derived from finer data, and this smoothing process is not exactly represented by the arbitrarily drawn boxes with no holes that appear in Figure 5. Finally, since the satellite is moving during the time of scan, later footprints are slightly advanced in the along-track direction. Due to differing sensor design, the SSC and OLS differ in their image motion during scanning. We speculate the combined effect of these uncertainties is on the order of 25 percent of the footprint size, that is, a colocated average visible or IR might have only 75 percent of its footprint over the corresponding SSC footprint. When data values were printed out near sharp cloud edges, cases could be found where one of the SSC or visible channels appeared filled with clouds while the other channel appeared only partly filled with clouds. This uncertainty contributes some noise to any analysis for automated classifications that is based on individual SSC and colocated OLS data. We have tried to reduce this noise by averaging  $4 \times 4$  arrays of SSC data in most of our analyses. This noise could be removed if the SSC channel were incorporated into the design of the OLS.

Our normalization of SSC and visible data is an attempt to make the greyscale of both directly proportional to scene reflectivity when the sun is overhead. Both the SSC and visible data were adjusted on the spacecraft for varying solar illumination by means of gain procedures discussed in Section 3.2. Our need to normalize arises in trying to use both channels for multi-spectral algorithms since the SSC and OLS gain procedures were not the same.

SSC and visible data were normalized to the geometry of an overhead sun by removing the gain factors listed in Tables 4 and 5 and substituting the factor  $1/\sin(\text{SSE})$ . In other words, the normalized brightness  $N$  is given by

$$N = \left( \frac{B}{G} \right) \cdot \frac{1}{\sin(\text{SSE})} \quad (5)$$

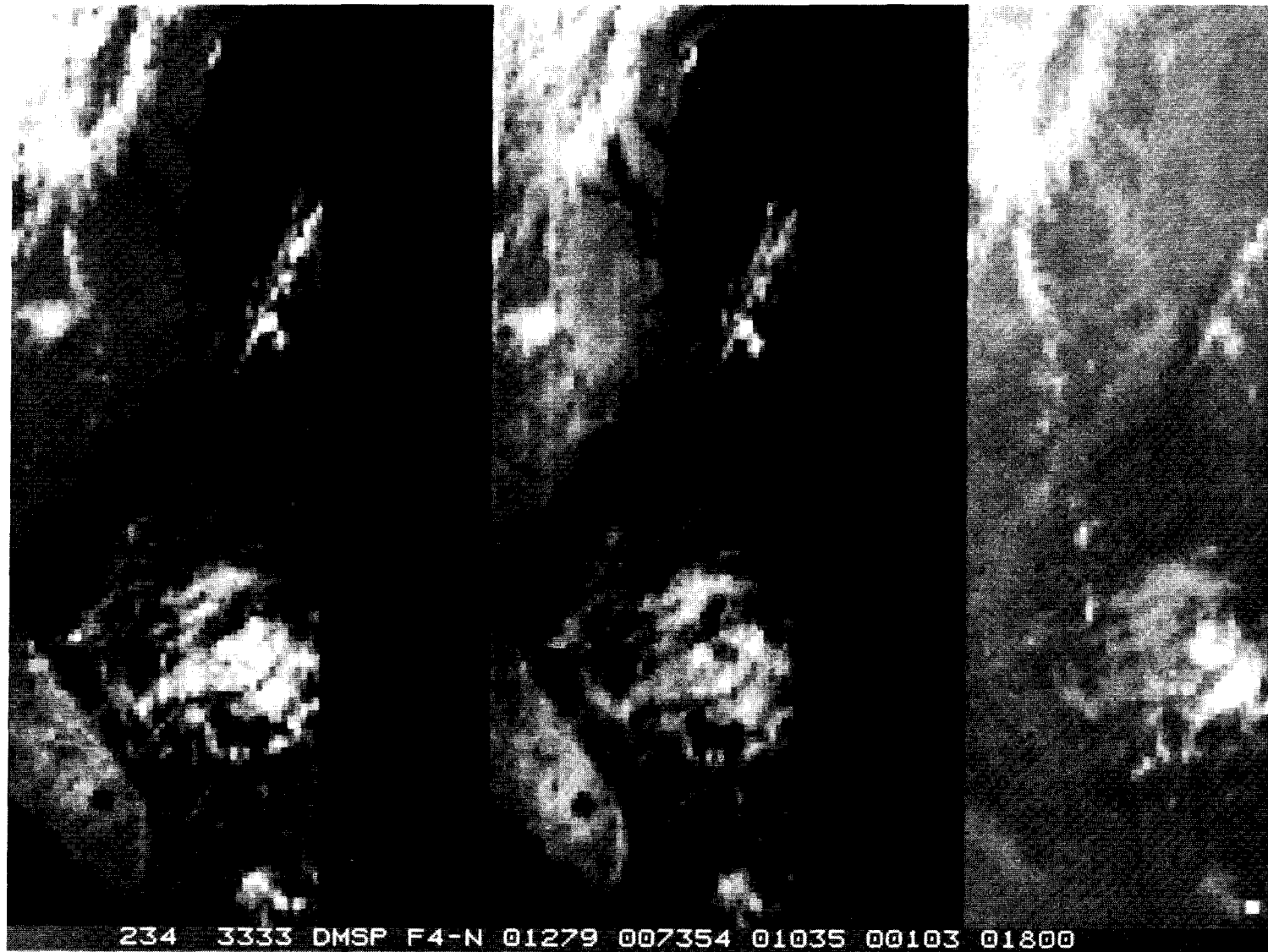


Figure 6. SSC Data (Center Strip) and Colocated Visible (Left) and IR (Right) as They Appear on the AFGL McIDAS at a Resolution of About 6 nmi. The Eastern U.S.A. coastline is easy to see in the visible and SSC Images. Clear land is usually more reflective in the SSC than it is in the visible. Data were taken on 12 December 1979

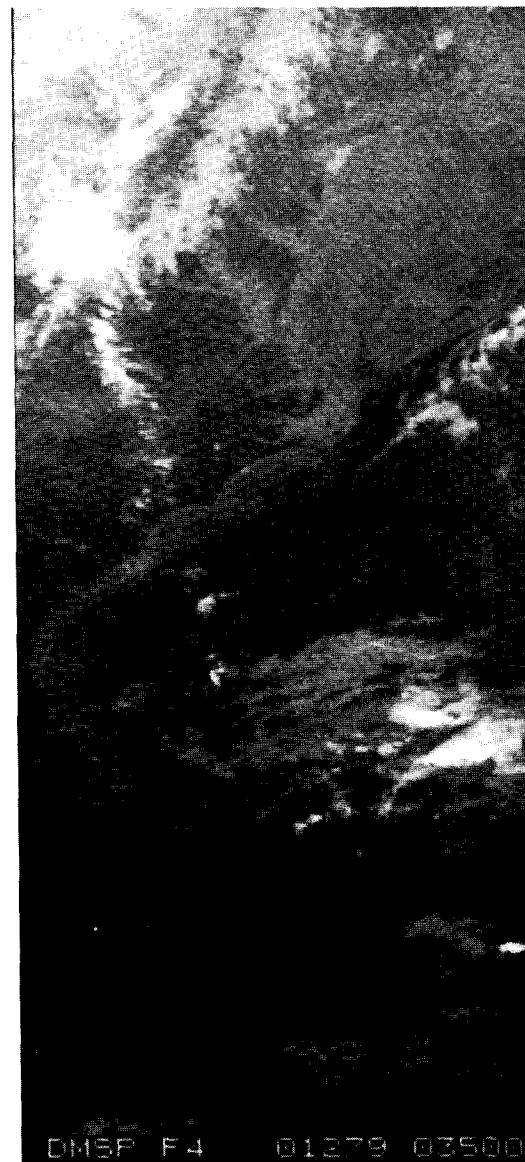
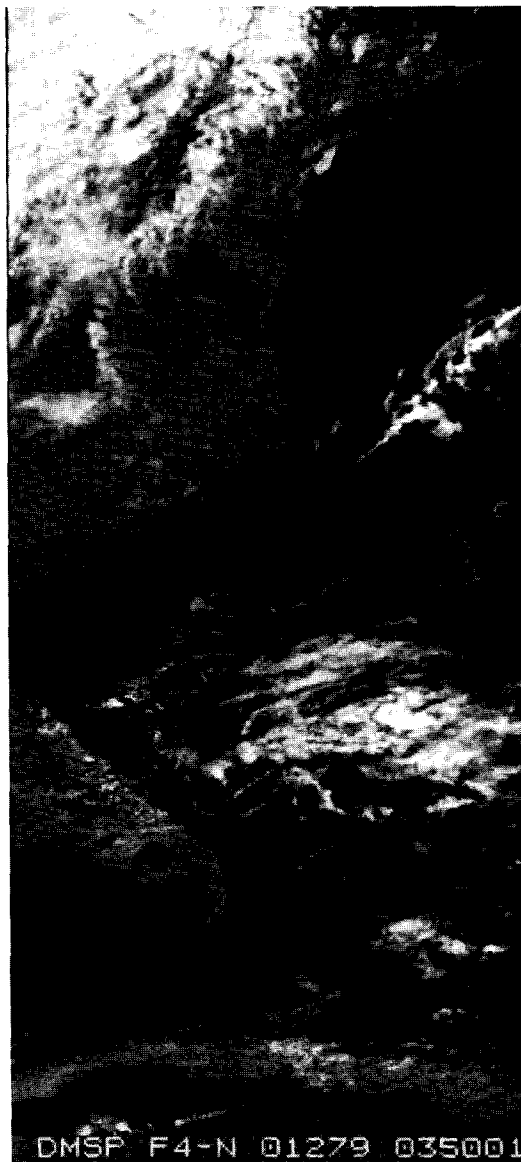


Figure 7. Visible (Left Strip) and IR (Right) at 3 nmi Resolution as They Appeared on the McIDAS. Different enhancement curves were used so that the land-ocean contrast is more prominent than in Figure 6. The 3 nmi data appear stretched in the east-west direction. (Compare Florida to Figure 6.) This occurs since McIDAS picture elements are square while the OLS footprints (see Figure 5) are shorter in the east-west direction

where B is the greyscale of either SSC or visible data provided by AFGWC, G is the gain ratio, and SSE stands for scene solar elevation.

When the sun is overhead, the visible sensor saturated for 80 percent of incident in-band solar energy; the SSC saturated for 51 percent in laboratory calibration and 53 percent for a post-flight analysis of instrument operating temperatures. Consequently, to make compatible OLS and SSC images we multiplied all SSC data from Eq. (5) by the factor  $(.51/.80)$  equal to 0.6375. When we were informed of the post-flight analysis that changed the SSC saturation to 53 percent, we had already generated our data base and were well into our analysis. Rather than duplicate efforts, we decided to continue analysis with the existing data base. The difference was too small to interfere with subjective analysis of SSC images and has had no known impact on the automated analysis. Proper reflectivities corresponding to the SSC data values are given in Table 8.

Table 8. Visible and SSC Greyscale and Corresponding Reflectivities Following Normalization by AFGL

Greyscale	Visible (OLS) Reflectivity	SSC Reflectivity First Calibration	SSC Reflectivity Recalibration
0	0	0	0
5	0.06	0.06	0.07
10	0.13	0.13	0.13
15	0.19	0.19	0.20
20	0.25	0.25	0.26
25	0.32	0.32	0.33
30	0.38	0.38	0.40
35	0.44	0.44	0.46
40	0.51	0.51	0.53
45	0.57	0.57	0.59
50	0.63	0.63	0.66
55	0.70	0.70	0.73
60	0.76	0.76	0.79
63	0.80	0.80	0.83

It is known that normalization using the factor  $1/\sin(\text{SSE})$  will make images appear too bright for the smallest values of SSE. The explanation is that using the factor is equivalent to assuming that all radiation to the viewed point is direct sunlight and that none is scattered by atmospheric molecules or aerosols. In the extreme of twilight, all radiation is scattered, none is direct, and the factor  $1/\sin(\text{SSE})$  is obviously not useful. Moreover, the extent of scattering for the OLS visible band is obviously greater than for the SSC band since Rayleigh scattering is inversely proportional to the 4th power of the wavelength. The decreased transmission at shorter wavelengths of the OLS visible band (Figure 1) is caused by Rayleigh scattering.

The smallest values of SSE that we used for automated analysis were in the range of 10 to 15 degrees, and we believe that our normalization procedure is adequate for these values. Extending the analysis to smaller values would most likely require a departure from the factor  $1/\sin(\text{SSE})$  toward the gain settings given in Table 5.

#### 4. IMAGE ANALYSIS

##### 4.1 Interactive Capabilities

The development of automated classifiers required a series of known cases that are often referred to as "ground truth" or "cloud truth" cases. It was necessary to find cases with water clouds, ice clouds, and no clouds so that cloud phase discrimination can be added to automated classifiers. We had planned to have a few aircraft flights under the satellite by the AFGL Cloud Physics C-130 to verify the phase of the clouds and estimate the particle size distributions. Unfortunately, due to power supply problems on the spacecraft, the SSC sensor was turned off on 29 December 1979, and the flights planned for early 1980 could have no corresponding satellite data. Consequently, all "truth" cases were found by subjective analysis of images displayed on the McIDAS along with weather station reports and topographic maps. The analysis used data which AFGWC had saved prior to 29 December 1979.

The data saves provided by AFGWC (Table 7) were quarter orbits from near the North Pole down to the Equator passing over Eastern Canada, the U.S.A., the Caribbean Sea, and Central America. In general, a good diversity of cases were available. There were clouds over both land and water backgrounds, tropical clouds as well as arctic clouds, and clear land, ocean, and snow cover scenes. Snow cover over the Eastern U.S.A. was abnormally sparse. (This was the winter in which the Olympics were held on man-made snow at Lake Placid, N.Y.). However, Canada had adequate snow cover for our purposes and we knew that Woronicz<sup>3</sup>

had studied snow cover over Eurasia and Antarctica as well as North America to distinguish snow from clouds using the SSC. The only other abnormality of the data sample was that relatively few cirrus and cirrostratus clouds could be found over land.

In the image analysis, SSC and colocated visible and IR data were displayed on the McIDAS as in Figure 6. These data are blown up by a factor of 3 so that the images are roughly the same scale as the 3 nmi visible and IR data which appear in Figure 7. The 3 nmi data were loaded into the McIDAS so that the operator could switch back and forth from SSC to 3 nmi data. This procedure was found to improve the selection of cases by detecting small-scale cloud features or landmarks that could not be seen at the resolution of the SSC data.

After viewing all the satellite data on the McIDAS, the classification system listed in Table 9 was adopted. Instead of three simple categories such as clear, water cloud, or ice cloud, this system has fifteen. There are three categories for clear scenes and six categories for cloudy scenes, which may be over either land or water backgrounds. There are several reasons for using this many categories. First of all, we attempted to get a diverse set of cases so that algorithms could be used globally, and this requires analysis for water, land, and snow cover. Second, we know that background brightness and temperature differ greatly from land to ocean backgrounds so that categories for partly cloudy scenes are also needed. Finally, having a detailed breakout of categories allows a better error analysis by pinpointing the types of clouds or backgrounds which are poorly handled by an automated classifier.

In the classification scheme (Table 9), clear categories include water, land, and snow-covered land. Clouds believed to be water clouds were arbitrarily categorized as stratus for unbroken clouds, stratocumulus for broken clouds, and cumulus for scattered or widely-scattered clouds. Clouds believed to be ice clouds were arbitrarily categorized as cumulonimbus clouds for high thick clouds that were expected to have precipitation beneath; as cirrostratus for wide-spread clouds that appeared thin; and as cirrus for scattered clouds that appeared thin. The cumulonimbus clouds might have water at low altitudes, but the radiation sensed by the satellite comes almost entirely from the ice particles.

Cases were assigned classifications based on all available data. We found that we could readily identify clear land, water, and snow cover data using the 3 nmi OLS data and reference maps. Clear water was the easiest since it was very dark and uniform in the visible or SSC channels. For clear land and snow cover, we used maps of topography, vegetation, and soil types found in standard

Table 9. Clear and Cloudy Categories

Type	Background	Number of Samples
Clear Water (CLW)	WATER	61
Clear Land (CLL)	LAND	85
Clear Snow (CLS)	LAND	36
Stratus (ST)	LAND	23
	WATER	23
Stratocumulus (SC)	LAND	9
	WATER	40
Cumulus (CU)	LAND	40
	WATER	41
Cirrus (CI)	LAND	8
	WATER	26
Cirrostratus (CS)	LAND	6
	WATER	16
Cumulonimbus (CB)	LAND	3
	WATER	16

atlases.<sup>27,28,29</sup> These allowed us to recognize such features as mountain ranges, forests, and frozen lakes that confirmed that no clouds were present.

Cloud phase was assigned to a cloudy area after a number of factors were considered. The size, shape, and texture of the clouds, particularly in the 3 nmi visible data, was a factor. Water-phase clouds often appear to have sharper edges than ice clouds since small water drops evaporate more efficiently at the side of a cloud. The source of the cloud can be important. Cold air blowing over warm water is expected to produce water clouds while thin clouds downwind of a cumulonimbus complex are expected to be ice clouds. The cloud motions were studied using GOES East visible and IR images at 30-minute intervals. IR temperatures have important, though limited, information on cloud phase. The IR temperature can be converted to an estimate of cloud top temperature by correcting for atmospheric attenuation. When the cloud top temperature is less than  $-40^{\circ}\text{C}$ , it is

27. The Times Atlas of the World, Mid-Century Edition (1957) The Americas, Vol. 5, Houghton Mifflin Co., Boston.
28. U.S. Department of the Interior (1970) The National Atlas of the U.S.A., Geological Survey, Washington, D.C.
29. Department of Mines and Technical Surveys (1957) Atlas of Canada, Geographical Branch, Ottawa, Canada.

assumed to be an ice cloud since supercooled water droplets are almost never observed below  $-40^{\circ}\text{C}$  (Curran and Wu<sup>30</sup> describe exceptions). When the IR temperature is above  $0^{\circ}\text{C}$ , the cloud can be assumed to be a water cloud unless it is a thin ice cloud. Clouds between  $0^{\circ}\text{C}$  and  $-40^{\circ}\text{C}$  may have water or ice particles.

Our subjective analysis of the SSC, IR, and visible images confirmed that the SSC was doing a good job of discriminating water clouds from ice clouds as theory has indicated and prior experiments have concluded. The image contrast between water clouds and ice clouds was much sharper in the SSC channel than in the visible or IR channels. We then concentrated on adding the cloud phase information to automated cloud decision algorithms.

The following procedures were used to select and verify cases. First, the 3 nmi visible and IR images were examined to find potential cases. Next, these cases were located on the SSC images. McIDAS interactive graphics will display a cursor of arbitrary size on the TV screen. A square cursor of  $12 \times 12$  picture elements, that is,  $4 \times 4$  of the blown up SSC data, was used in the analysis since it encloses a ground area of about  $25 \times 25$  nmi, which is the current unit of analysis for the 3DNEPH. Identical squares were drawn on the smoothed and colocated visible and IR data, which appear on either side of the SSC strips (Figure 6). The earth location of the cursor was then determined by the McIDAS and reference maps were consulted if the area was over land or near a coastline. Next, a special command (SM) was executed to save and classify the three arrays of SSC, visible and IR data. The image analyst would key in the clear or cloud classification from Table 9 along with the type of background. The McIDAS command would transfer the digital data under the cursor squares to digital disk storage reserved for this project. Bookkeeping information such as the orbit number and line and element identification were automatically saved along with the  $4 \times 4$  arrays of colocated SSC, visible, and IR data. All cases were checked by recalling the data arrays from the disk and displaying the numbers on a separate McIDAS console. This procedure was found to be helpful to check for proper entry of classification and background codes, for bad scan-lines, questionable collocation of data, and to ensure that mixed-phase clouds or coastlines were not present. If the checks revealed a questionable case, it was deleted from the disk file. Most of the cases were examined by both authors of this report. The automated analysis described later used only the saved arrays of SSC and colocated visible and IR data. The 3 nmi data were used only for image analysis.

---

30. Curran, R. J., and Wu, M-L. (1981) Identification from space of water droplet clouds at temperatures below  $-40^{\circ}\text{C}$ , J. Atmos. Sci. (in press).

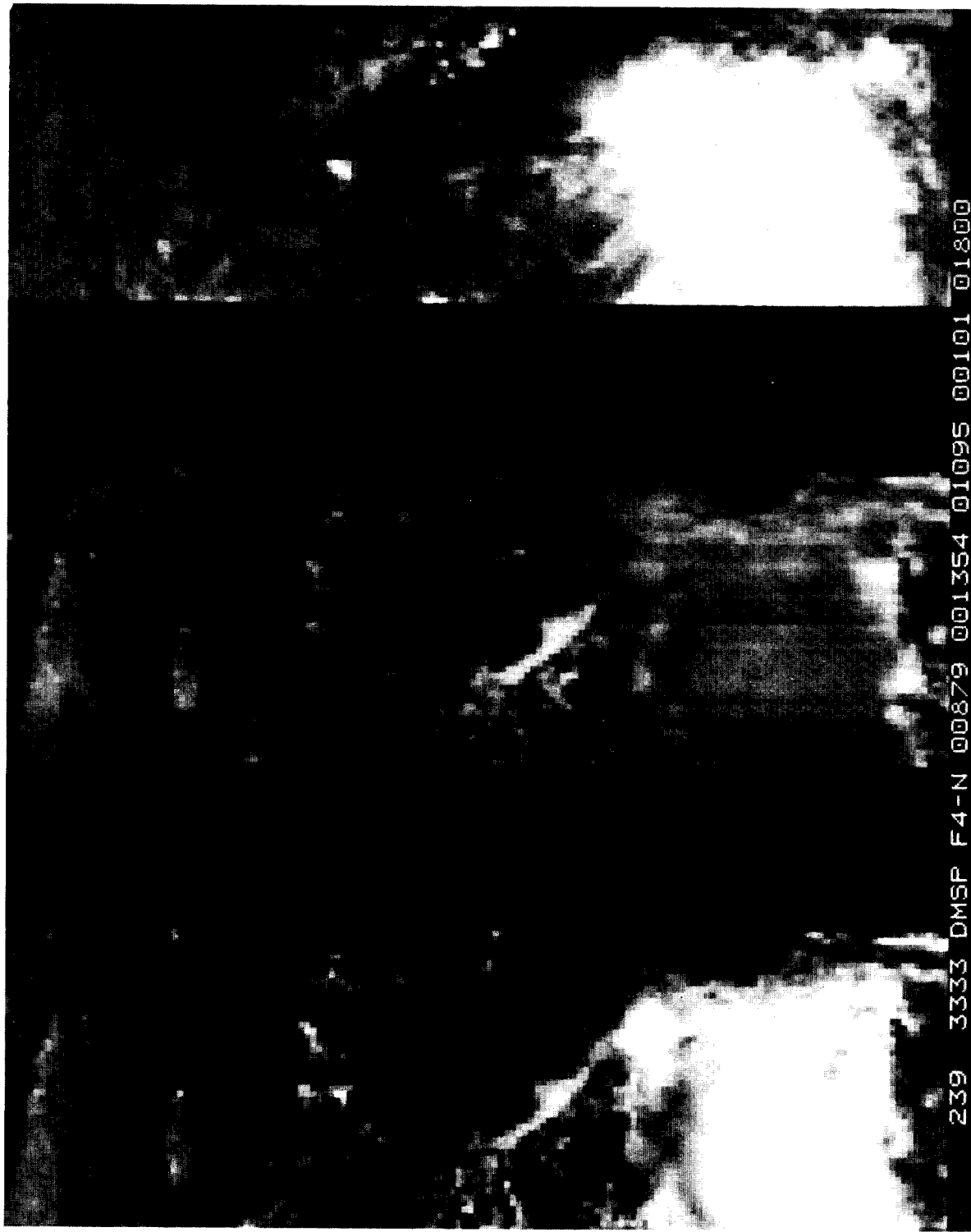
## 4.2 Examples

Many significant properties of the near-IR SSC channel were obvious in the image analysis. They are briefly described here by means of examples and comments while the numerical analysis is given in subsequent sections of this report.

Figure 8 has low-latitude coverage for the 8 December orbit. The eastern half of Cuba is at the top of the images and Columbia, South America, is in the clear on the lower right of the images. Cloud-free oceans are dark in both visible and SSC images and the clear/cloud contrast is good. Clear land in Columbia, Jamaica, Haiti, and Cuba is generally more reflective in the SSC than in the visible channel in this case and all others. A large complex of cumulonimbus clouds is in the lower left of the images. They are very good reflectors in the visible and poor emitters (that is, cold) in the IR. However, since the satellite is sensing the ice particles in the upper part of the cumulonimbus clouds, they are poor reflectors in the SSC channel and appear dark. The area of cold IR temperatures is much larger than the bright area in the visible. The difference represents cirrus clouds blown north from the centers of convective activity. The SSC reflectivity varies little over the cumulonimbus and cirrus blowoff even though the cloud thickness varies greatly; the grey appearance or weak reflectivity of these clouds is an excellent indicator of the ice phase. It is important, however, to utilize either the visible or IR data to make an unambiguous designation of ice clouds since the reflectivity of ice clouds is nearly the same as clear land. The SSC view of cumulonimbus and cirrus shows some vertical striping in an otherwise uniform scene. The stripes are caused by small (about 2 out of 64 greyscale) variations between detectors in the SSC array of 48 detector elements.

Figure 8 also has cumulus clouds over water in the middle-left of the images. They are water-phase clouds and are good reflectors in both visible and SSC channels, but are barely detectable in the IR channel due to their relatively warm temperatures. There are also some cumulus clouds over Cuba and Jamaica. The cumulus clouds are easier to see in the 3 nmi data (Figure 9).

A large area of cirrus and cirrostratus clouds appears in the center of Figure 10 (SSC data) and Figure 11 (3 nmi data). These clouds are associated with a nearly-stationary front over the ocean. The bumpy texture of the visible picture indicates some lower clouds under the cirrostratus. The SSC image of the cirrostratus is nearly uniform in appearance since these clouds, like the cumulonimbus, are poor reflectors. The water-phase stratocumulus clouds lying to the north of the ice clouds are highly reflective in both visible and SSC channels. Over the ocean, all high reflectivity scenes are water clouds except for the particular viewing geometry which produces sunglint.



239 3333 DMSP F4-N 00879 001354 01095 00101 01800

Figure 8. SSC Data (Center) and Colocated Visible (Left) and IR (Right) for 8 December 1979

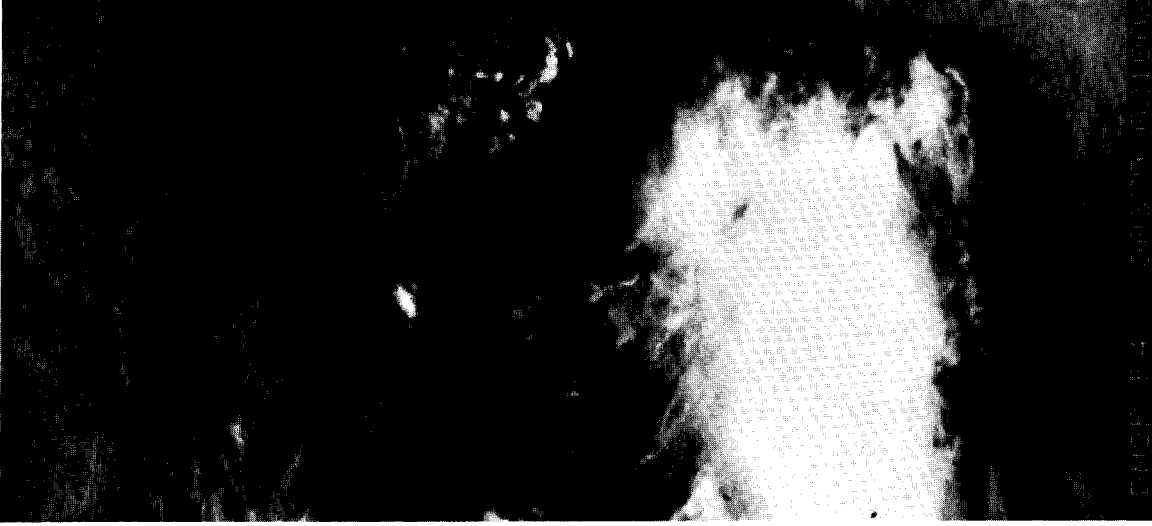


Figure 9. Visible (Left) and IR (Right) Data at 3 nmi for the Locations Shown in Figure 8

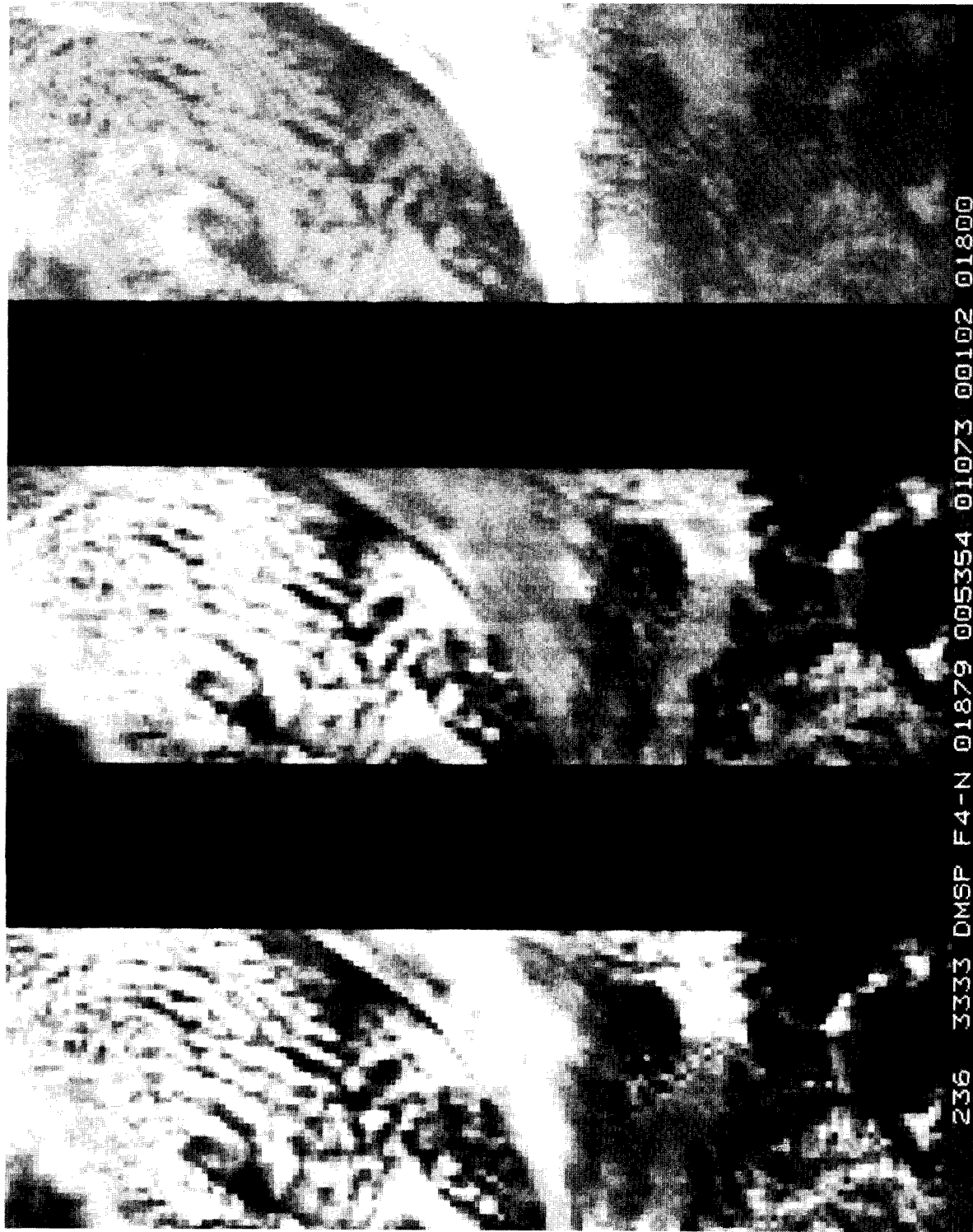


Figure 10. SSC Data (Center), Colocated Visible (Left), and IR (Right) for 18 December 1979. Cirrostratus clouds are in the center and stratocumulus clouds are at the top of the images



Figure 11. Visible (Left) and IR (Right) Data at 3 nmi for the Locations Shown in Figure 10

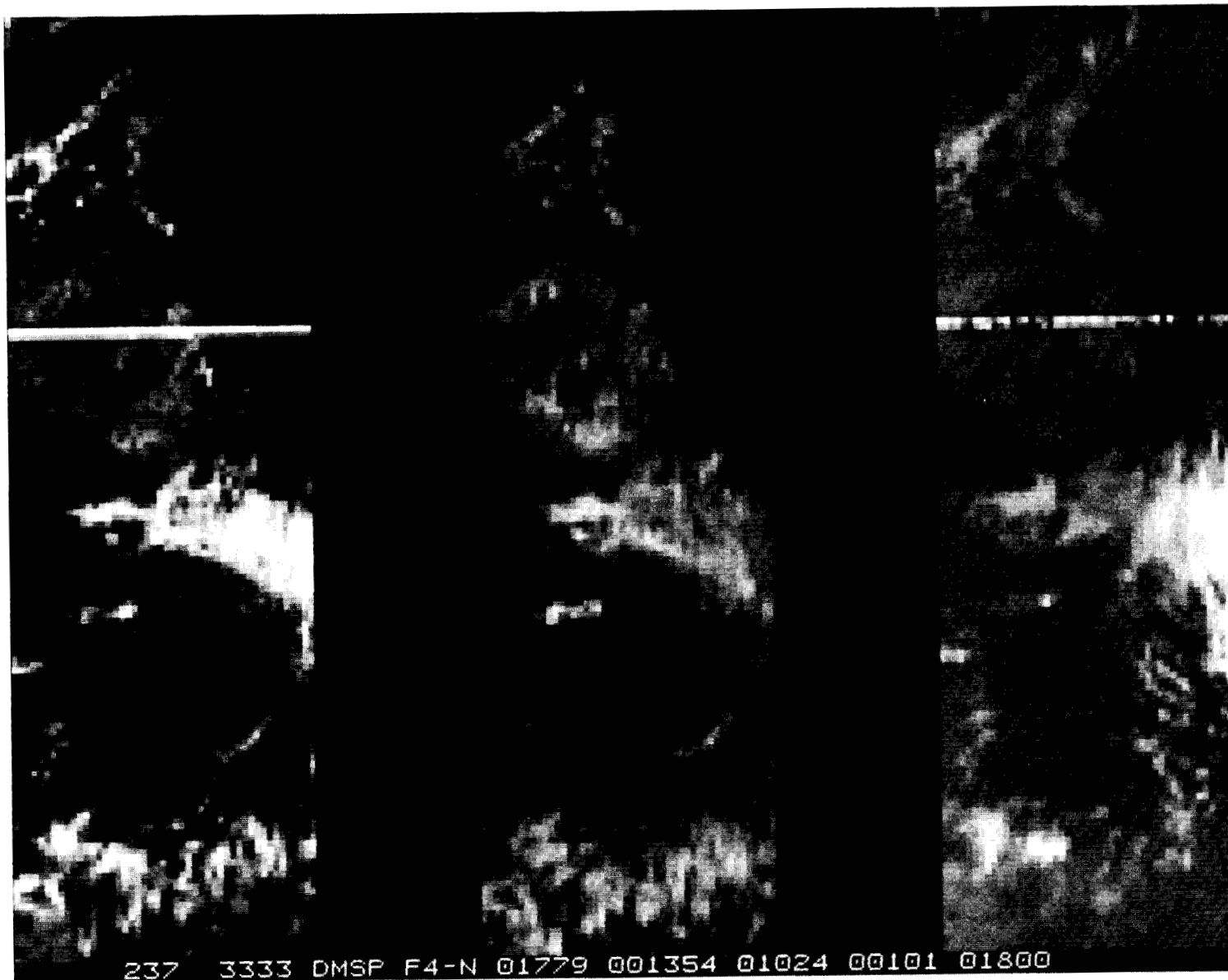


Figure 12. SSC Data (Center), Colocated Visible (Left), and IR (Right) for 17 December 1979. Nicaragua appears in the center of the images

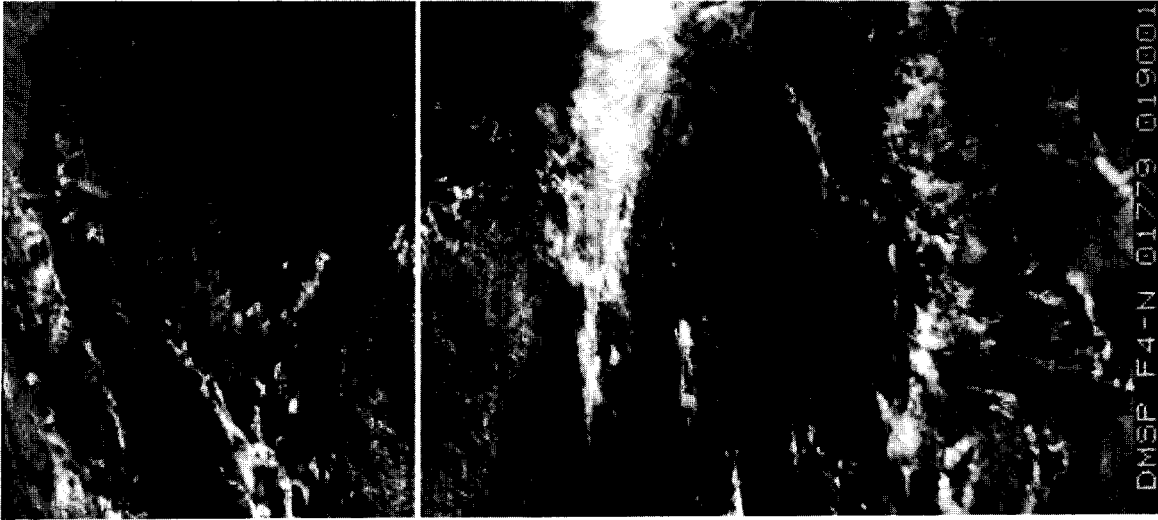


Figure 13. Visible (Left) and IR (Right) Data at 3 nmi for the Locations Shown in Figure 12



Figure 14. SSC Data (Center), Colocated Visible (Left), and IR (Right) for 27 December 1979. Cirrus clouds are over south-central Florida. To the north, the land is clear. Considerable variation in the SSC reflectivity over land can be seen in northern Florida, Georgia, and the Carolinas

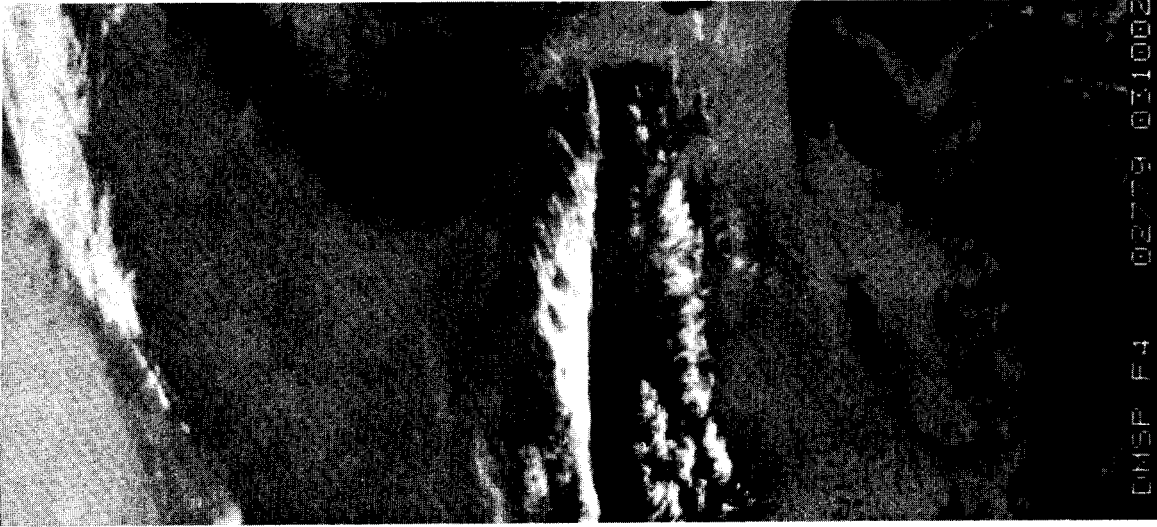


Figure 15. Visible (Left) and IR (Right) Data at 3 nmi for the Locations Shown in Figure 14



Figure 16. SSC Data (Center), Colocated Visible (Left), and IR (Right) for 17 December 1979. Forests and lakes covered by snow are in the upper-left of the images

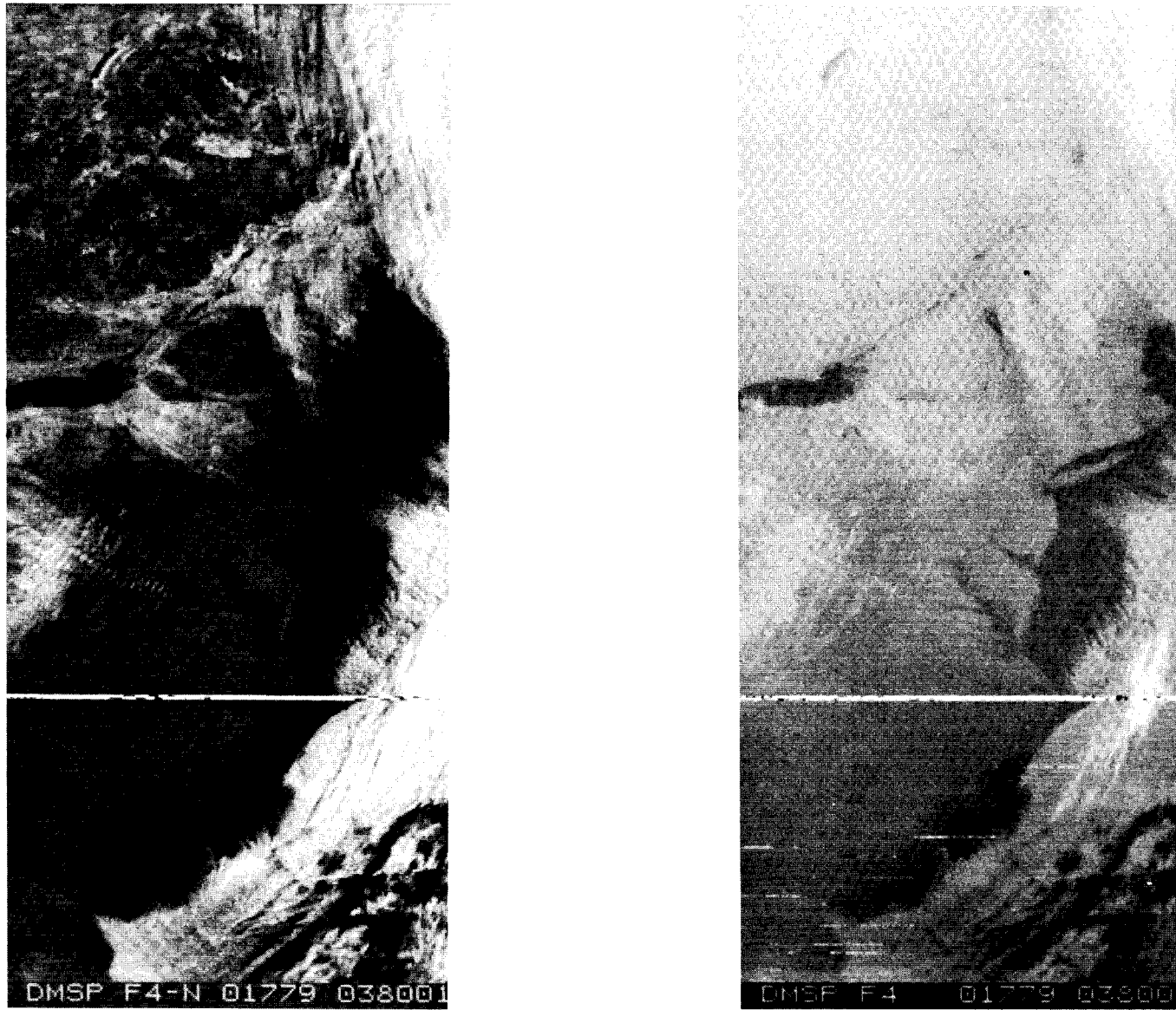


Figure 17. Visible (Left) and IR (Right) Data at 3 nmi for the Locations Shown in Figure 16

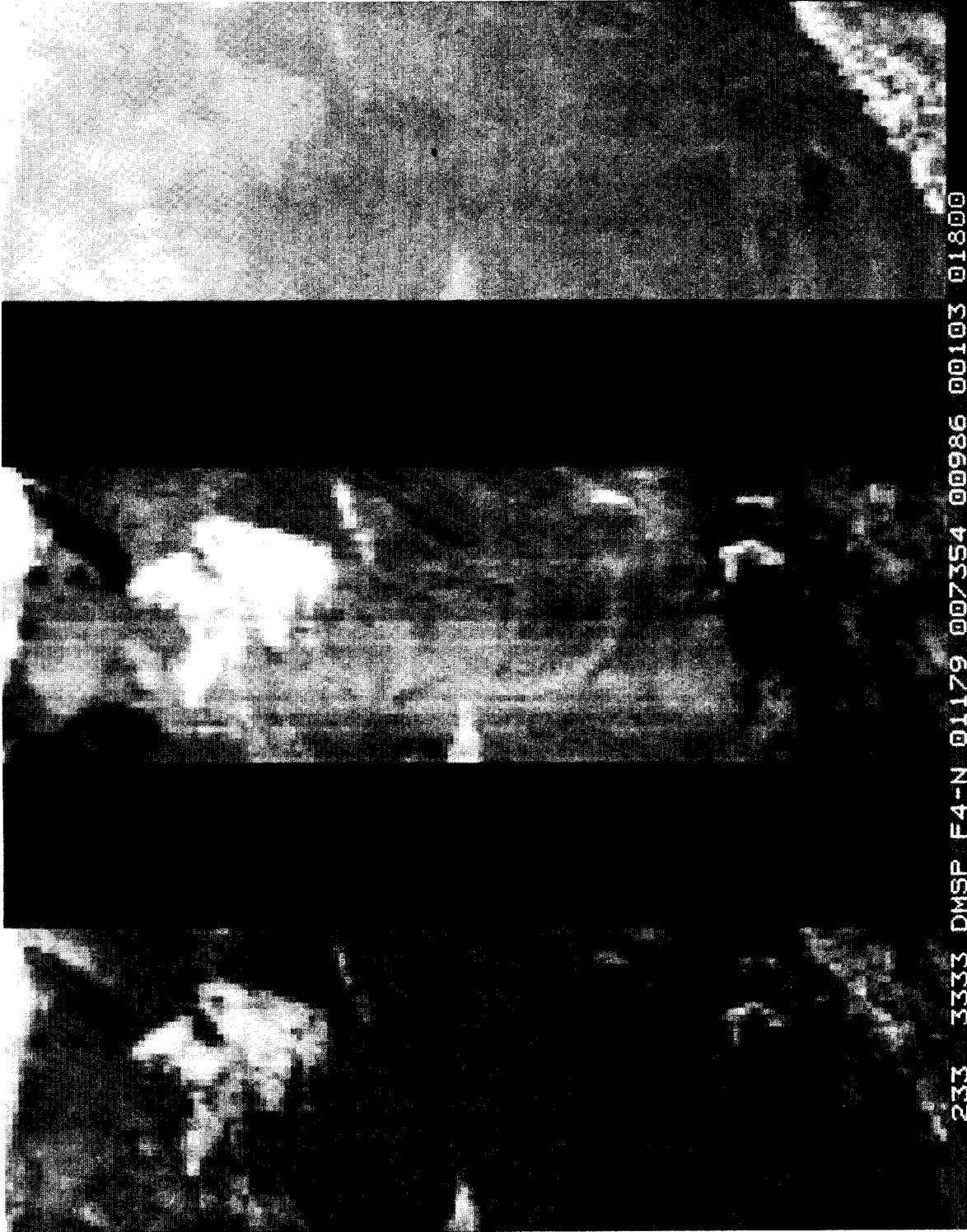


Figure 18. SSC Data (Center), Colocated Visible (Left), and IR (Right) for 11 December 1979. Lake Erie is near the top of the images and the Gulf of Mexico is at the bottom

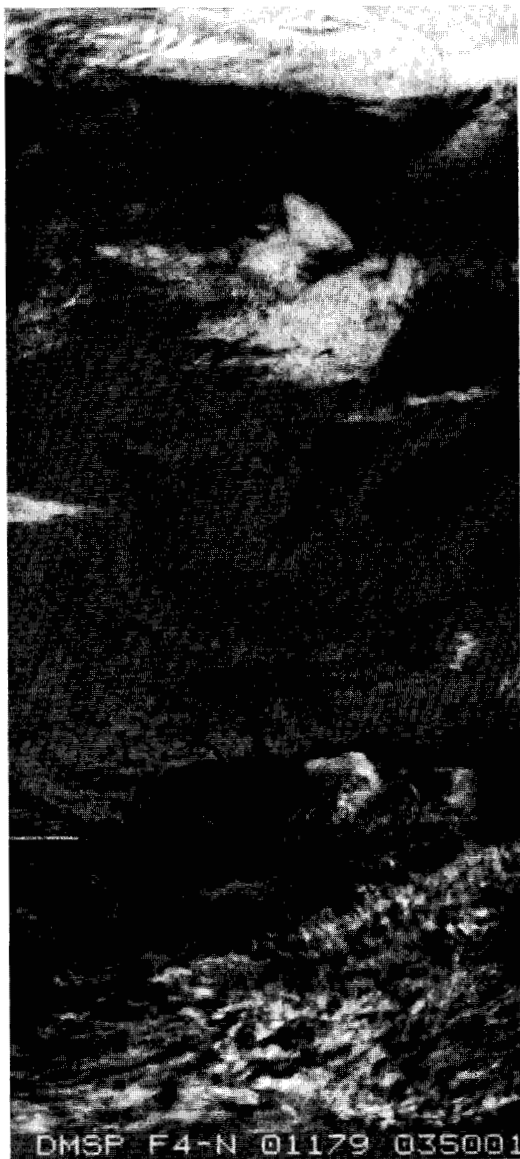


Figure 19. Visible (Left) and IR (Right) Data at 3 nmi for the Locations Shown in Figure 18

Cumulus clouds over land (Honduras and Nicaragua) appear in Figures 12 and 13 near the center of the images. Despite the fact that the SSC resolution was coarse, cumulus clouds were generally easy to spot over land backgrounds. Moreover, the higher reflectivities of land backgrounds in the SSC spectral region did not hinder cumulus detection. Unlike ice clouds, water clouds were detectable in the SSC images without the need to reference another channel such as the IR.

Figures 14 and 15 show water clouds (stratocumulus) south of Florida and ice clouds (cirrus) near and over central Florida. North of the cirrus clouds, the clear land of Florida, Georgia, and the Carolinas shows significant reflectivity variations in the SSC. In the visible data, the reflectivity of the clear land varies much less.

The SSC data in Figure 14 show surface variations in reflectivity which have attracted interest for remote sensing of vegetation and soil types. (References are given in Section 2.) The National Atlas of the U.S.A. <sup>28</sup> shows that the Gulf-Atlantic Rolling Plain parallels the Carolinas, the Georgia Coast, and eventually extends downward into the western side of the Florida Peninsula. The location of the Gulf-Atlantic Rolling Plain agrees very well with the brighter land in the SSC image. The darker shades of land are the Gulf-Atlantic Coastal Flats. Other maps in the National Atlas show that the bright land in Florida has relatively more sandy soil and relatively less open water or marsh than the darker land to the east.

Figures 16 and 17 have a good variety of clear and cloudy scenes. The upper-left parts of the images have clear skies and snow cover is visible from Lake Ontario and the St. Lawrence Valley northward. There is also some snow south of Lake Ontario. In the SSC image, the cloud/snow contrast is excellent for the water clouds southeast of Lake Ontario, over the mountains of Vermont and New Hampshire, and for the stratus clouds over Maine. The cloud/snow contrast is good for some thin cirrus clouds in the upper right of the images. The snow-covered land is darker than the snow-free land such as Massachusetts, Delaware, and the states to the south. By comparing the visible and SSC images alone, the cloud/snow discrimination is much better than in the better-resolution 3 nmi visible and IR images which show more landmarks.

Figures 16 and 17 also show some wave clouds over the Appalachian Mountains that are probably a mixture of ice and water clouds since the SSC reflectivity is highly variable. There are also water-phase stratus and stratocumulus clouds off the East Coast.

Figures 18 and 19 show another orbit with snow and clouds. Low water clouds cover parts of Indiana and Ohio. They are easy to detect in the SSC image. A thin snow cover due to lake-effect snowfall can be seen just southeast of Lake Erie. It is darker than the surrounding snow-free land and easy to detect when the SSC and visible images are compared.

When only visible and IR data are available, snow/cloud discrimination is often difficult in subjective image analysis and is even more difficult in automated analysis. Figure 17 has locations where subjective snow/cloud discrimination cannot be done without also looking at the SSC image in Figure 16. Figure 19 is easier to discriminate subjectively. The low clouds over Indiana and Ohio do not have the shape of a snow swath laid down by a storm since they terminate abruptly on the northeast side. On the other hand, lake-effect snow cover is expected on the southeast side of Lake Erie, and the clear shoreline confirms that clouds are absent. These lines of reasoning are not, however, available to the AFGWC automated cloud analysis, and the snow would be confused with clouds. Consequently, visible data are not used for automated cloud detection where snow cover may be present. Therefore, the SSC channel is expected to improve automated analysis since the snow/cloud contrast is great.

## 5. AUTOMATED CLOUD CLASSIFICATION

Previous studies have suggested decision rules for discriminating water clouds from ice clouds and for discriminating clouds from snow cover. Four of these rules are briefly described in this section and are tested against the 433 cases that were classified by image analysis. Results appear in the next section. Several forms of a minimum distance classifier are also described and tested. The following discussion of decision rules proceeds chronologically from the earliest to the most recent.

Several studies have suggested using the ratio of an SSC channel to a visible channel as a useful parameter for cloud phase and cloud/snow-cover discrimination. If the SSC channel measurement is put in the numerator so that SSC/visible is defined as the ratio, then the lowest values are expected for snow cover, the highest values are expected for water clouds, and ice clouds would have intermediate values. The ratio is useful since it is expected to be insensitive to variations in solar illumination and scattering geometry. Clouds vary in reflectivity due to variations in depth as well as width and the use of a reflectance may also be insensitive to these cloud size variations if the two channels see the same field of view. Finally, the ratio is simple enough to be a candidate for data processing on the satellite which could ease the burden of storing and transmitting complete data records from a new channel. NASA scientists<sup>10</sup> have suggested that the ratios should only be used if the clouds exceed a certain optical thickness for visible measurements; above a given optical thickness, cloud phase discrimination is more accurate and fewer clear areas are mistakenly identified as clouds. We arbitrarily used a visible greyscale of 9, corresponding to a reflectivity of about 11 percent, as a lower bound when ratios were calculated.

A decision tree for discriminating snow cover, ice clouds, water clouds, and other cloud-free surfaces was suggested by Hunt et al<sup>4</sup> based on a review of literature available to 1974. The decision tree is shown in Figure 20. The decision tree starts like the visible processor of the 3DNEPH with a critical visible greyshade to distinguish the dark/clear scenes from all others. In the 3DNEPH,<sup>24</sup> the

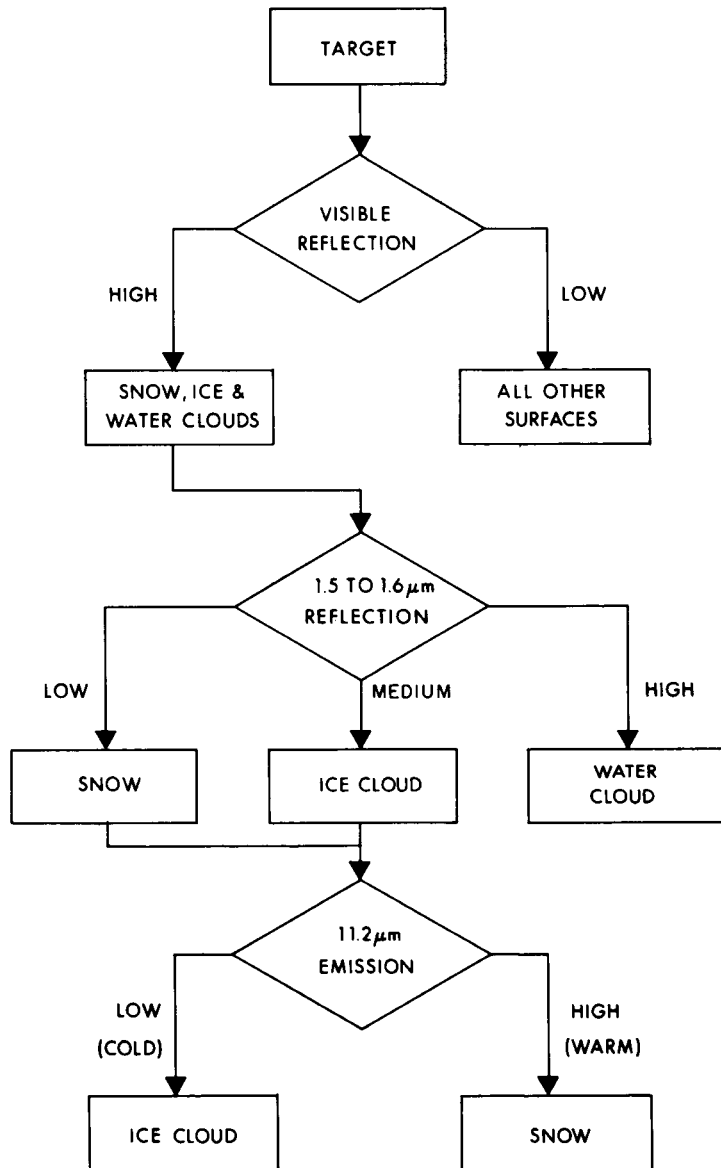


Figure 20. Decision Tree Suggested by Hunt et al<sup>4</sup> for Classifying Water Clouds, Ice Clouds, Snow Cover, and Other Cloud-Free Surfaces

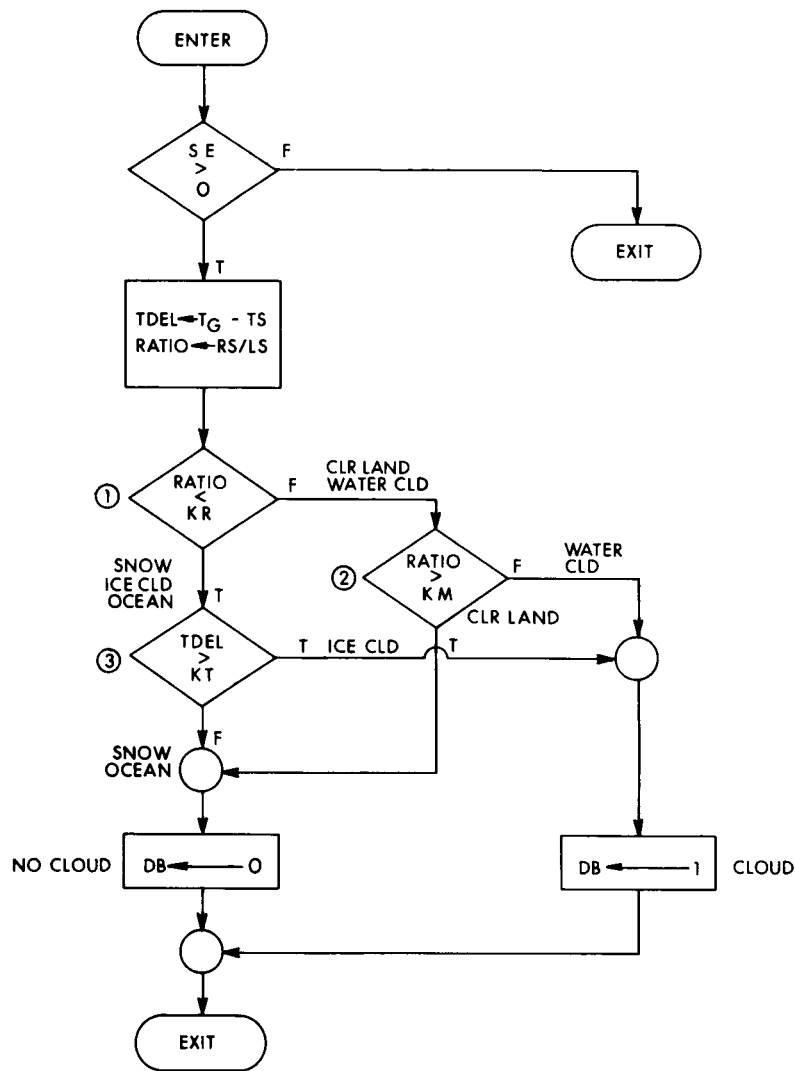
visible greyscale for clear/cloud decisions varies with earth-location, that is, land backgrounds are brighter than ocean backgrounds, and also the land backgrounds change during the course of the year. The 3DNEPH background fields could be applied to the first decision of this tree. The SSC channel would next be used to discriminate snow cover, ice clouds, and water clouds. Based on the limited spectroscopic measurements available, the authors suspected that some ice clouds would be confused with snow cover. A thermal IR measurement was added to double check the discrimination of ice clouds and snow. The exact logic to combine the IR and SSC information was not specified in the report. This decision tree uses no ratios so it assumes that the reflected sunlight channels (visible and SSC) have been normalized to some standard level of illumination. It also assumes that critical thresholds can be found for all three channels. This decision tree was intended to provide improved snow/cloud discrimination, since earlier studies were primarily concerned with cloud phase.

Kimball<sup>23</sup> proposed an algorithm based on his analysis of the SSC instrument and some data samples. His decision tree is shown in Figure 21. The objective was an algorithm suitable for onboard processing, to discriminate cloudy scenes from cloud-free scenes including snow cover. The resulting cloud/no cloud decision would compress the SSC data from six bits down to one bit, which could be readily stored and transmitted by the spacecraft. Some information as to the ground temperature would have to be uplinked to the spacecraft. Critical thresholds of the ratio SSC/visible (RS/LS in Figure 21) would have to be provided to the spacecraft processor.

Kimball<sup>23</sup> described his algorithm as preliminary and in need of global testing. We modified his ratio by inverting it from visible/SSC to SSC/visible since zero values of SSC were occasionally observed over clear oceans. Since we were concerned that this algorithm might not work over clear water backgrounds, we tested on land cases only as well as all land and water cases together.

Woronicz<sup>3</sup> developed a decision matrix using SSC and visible measurements to distinguish clear, snow cover, and cloudy scenes. His decision matrix is shown as the dashed lines in Figure 22. These lines were determined by examining many cases of SSC data compared to 3 nmi visible and IR data. Any amount of cloud within the SSC FOV, even a single 3 nmi pixel, was considered a cloudy case. Similarly, any amount of snow within a clear FOV was considered a snow cover case. Mixed cloud and snow scenes were treated as cloudy cases.

The hypothesis tested in the Woronicz<sup>3</sup> study was discriminating snow cover from cloud cover using a combination of SSC and OLS data. Discriminating snow cover can improve not only the 3DNEPH,<sup>24</sup> but also the separate snow cover model



LEGEND  
 CLD = CLOUD  
 CLR = CLEAR  
 KM, KR, KT = THRESHOLD LEVELS  
 LS = LIGHT (VISIBLE) OLS  
 RS = SSC CHANNEL  
 TG = GROUND TEMPERATURE  
 TS = THERMAL (IR) OLS  
 SE = SOLAR ELEVATION

Figure 21. Decision Tree Suggested by Kimball<sup>23</sup> for Discriminating Cloudy from Cloud-Free Surfaces Including Snow Cover

(SNODEP<sup>31</sup>) maintained by AFGWC. The Woronicz<sup>3</sup> study used a wider range of cases than were used in the present study. In particular, SSC data were examined over bright arid terrain features and snow cover over Eurasia and Antarctica. The decision matrix was tested over large areas of four different orbits. The area covered in this test is about seven times as great as the area covered by our 433 cases. The verification rates are reproduced in Table 10. They are very good, with a 90.1 percent correct classification for cloud/no cloud decisions and 88.7 percent for three-way classification into clear, snow cover, and cloudy categories.

31. Luces, S. A., Hall, S., and Martens, J. (1975) The AFGWC Snow Cover Analysis Model, AFGWC Technical Memorandum 75-1.

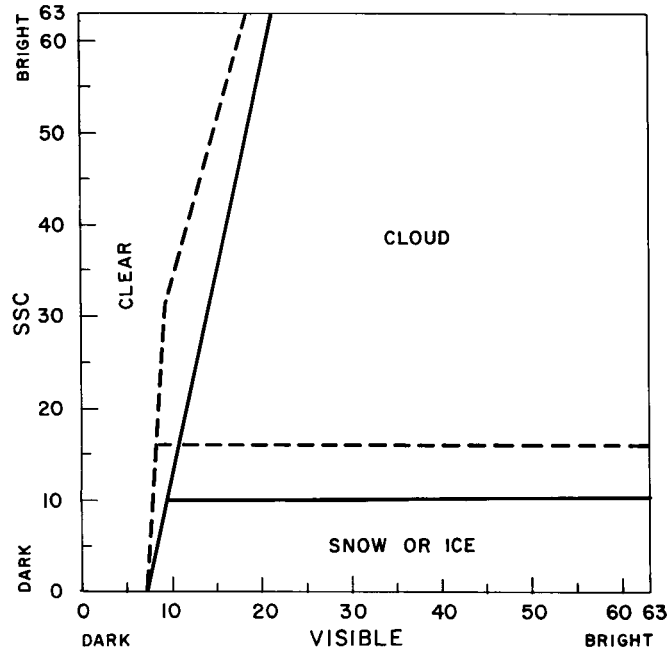


Figure 22. Decision Matrix by Woronicz<sup>3</sup> (Dashed Lines) Modified to Our Normalized Values of SSC (Solid Lines)

Table 10. AFGWC Test of Decision Matrix Given in Figure 22

		Automated		
		Clear	Snow	Cloud
Observed	Clear	92.4%	1.3%	6.3%
	Snow	10.3%	81.9%	7.8%
	Cloud	4.6%	6.1%	89.3%
Reliability of cloud/no cloud decisions		= 90.1 percent		
Reliability of clear/snow/cloud decisions		= 88.7 percent		

We tested the Woronicz<sup>3</sup> decision matrix against our own cases and also divided the cloud category into ice clouds and water clouds. Since we had normalized and, in doing so, generally reduced the values of our SSC greyscale we adapted his decision matrix boundaries (dashed lines) to be comparable to our SSC greyscale. The revised boundaries are the solid lines in Figure 22.

The decision rules that have been presented are all based on physical arguments or experimental data; however, they are all fairly simple to understand and to program on a computer. With a large and accurate data base, it is possible to test more complicated algorithms that may yield more accurate decisions. A number of studies have been made applying such algorithms to cloud type classification using visible, IR, or both forms of satellite data. They are summarized in an earlier report<sup>32</sup> and the statistical concepts are explained in a textbook by Duda and Hart.<sup>33</sup>

From the many possible approaches, we have chosen several forms of a minimum distance classifier. The forms generally discriminate categories by attempting to carve a visible-IR-SSC space into mutually exclusive three-dimensional cloud category regions. Three minimum distance classifiers were tested on our data base: unnormalized, normalized, and unnormalized with standard deviations.

The unnormalized minimum distance classifier uses the following discriminant function:

$$m_i(x) = ||x - \mu_i||, \quad i = 1, 2, 3, \dots, 9, \quad (6)$$

where  $x$  is a 3-component column vector  $\begin{bmatrix} x_1 \\ x_2 \\ x_3 \end{bmatrix}$  consisting of an observed sample's visible ( $x_1$ ), IR ( $x_2$ ), and SSC ( $x_3$ ) means;  $\mu_i$  is the mean of all  $x$ , category  $i$ ;  $i = 1, 2, 3, \dots, 9$  refers to the clear and cloud categories in Table 9. The notation  $|| \quad ||$  denotes the Euclidean distance from  $x$  to  $\mu_i$ , and is defined as  $(x - \mu_i)^t (x - \mu_i)$  ( $t$  denotes transpose). Rewriting Eq. (6),

---

32. Bunting, J. T., and Fournier, R. F. (1980) Tests of Spectral Cloud Classification Using DMSP Fine Mode Satellite Data, AFGL-TR-80-0181, ADA 094119.

33. Duda, R. O., and Hart, P. E. (1973) Pattern Classification and Scene Analysis, John Wiley & Sons, New York.

$$\begin{aligned}
m_i(\mathbf{x}) &= \|\mathbf{x} - \mu_i\|^2 \\
&= (\mathbf{x} - \mu_i)^t (\mathbf{x} - \mu_i) \\
&= \begin{bmatrix} (x_1 - \mu_1^i) & (x_2 - \mu_2^i) & (x_3 - \mu_3^i) \end{bmatrix} \cdot \begin{bmatrix} (x_1 - \mu_1^i) \\ (x_2 - \mu_2^i) \\ (x_3 - \mu_3^i) \end{bmatrix} \\
&= \sum_{n=1}^3 (x_n - \mu_n^i)^2, \quad i = 1, 2, 3, \dots, 9, \tag{7}
\end{aligned}$$

where  $\mu_n^i$  is the mean of all  $x_n$ , class  $i$  (from  $\mu_i$ ). The  $\mu_i$  are calculated from the cloud truth set prior to using Eq. (7). An  $m_i$  is calculated for all  $i$  and cloud type  $k$  is chosen such that  $m_k < m_i$  for all  $i \neq k$ .

In three dimensions with visible brightness counts on the x-axis, IR on the y-axis, and SSC on the z-axis (see Figure 23),  $m_i(\mathbf{x})$  is a measure of the linear distance between the ordered triples  $(x_1, x_2, x_3)$  and  $(\mu_1^i, \mu_2^i, \mu_3^i)$ . Equation (7) chooses the  $i$  for which  $m_i$  is smallest. Thus, Eq. (7) is for this reason called a minimum distance classifier. Cloud category  $k$  is chosen by Eq. (7) if  $(x_1, x_2, x_3)$  is closest spatially to  $(\mu_1^k, \mu_2^k, \mu_3^k)$ . If the  $\mu_i$  are all thought of as "ideal" mean vectors of category  $i$ , then Eq. (7) picks the cloud category whose mean vector  $\mu_i$  most closely resembles  $\mathbf{x}$  in a least-squared sense.

The normalized minimum distance classifier is defined as

$$d_i(\mathbf{x}) = \sum_{n=1}^3 \frac{(x_n - \mu_n^i)^2}{(\sigma_n^i)^2}, \quad i = 1, 2, 3, \dots, 9, \tag{8}$$

where  $\mathbf{x}$ ,  $x_n$ ,  $\mu_n^i$ ,  $i$ , and  $n$  are as previously defined;  $\sigma_n^i$  is the overall average standard deviation for cloud category  $i$ , imagery type  $n$ . Equation (8) is an equivalent form of a Bayes decision rule which is derived from the multivariate normal density. Hence  $d_i$  is a measure of the probability of a sample's being category  $i$  given the sample's mean column vector  $\mathbf{x}$ . A  $d_i$  is calculated for all  $i$ , and cloud type  $k$  is chosen such that  $d_k < d_i$  for all  $i \neq k$ . Derivation of discriminant functions

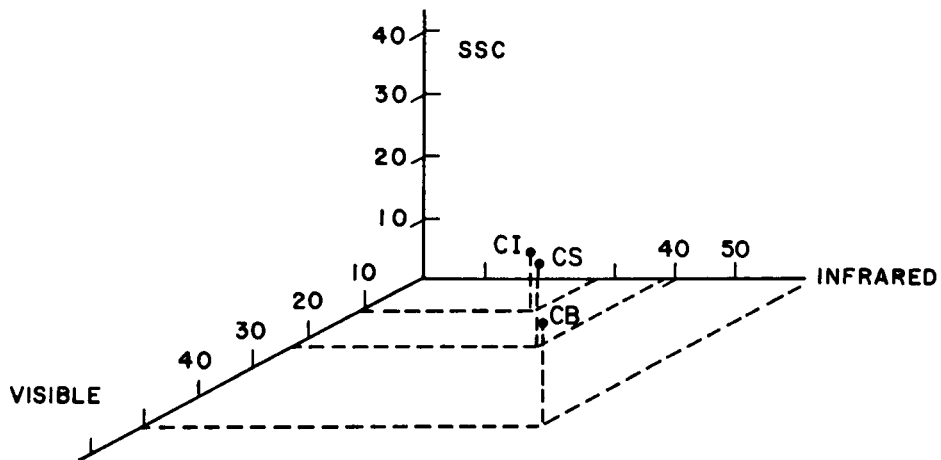
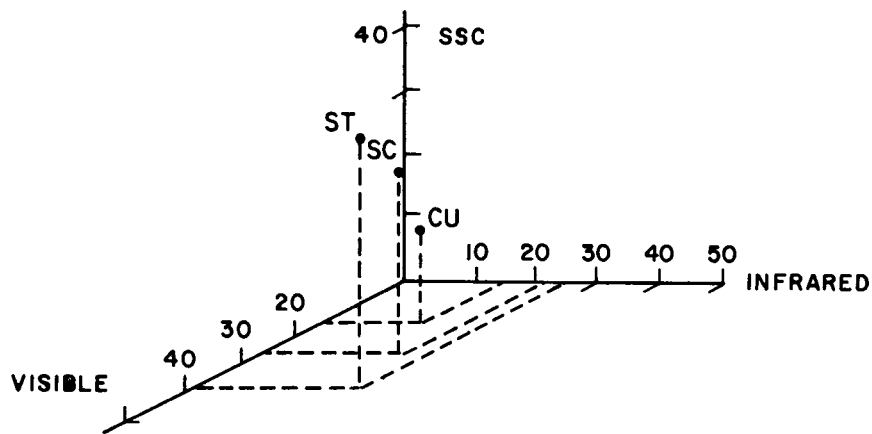
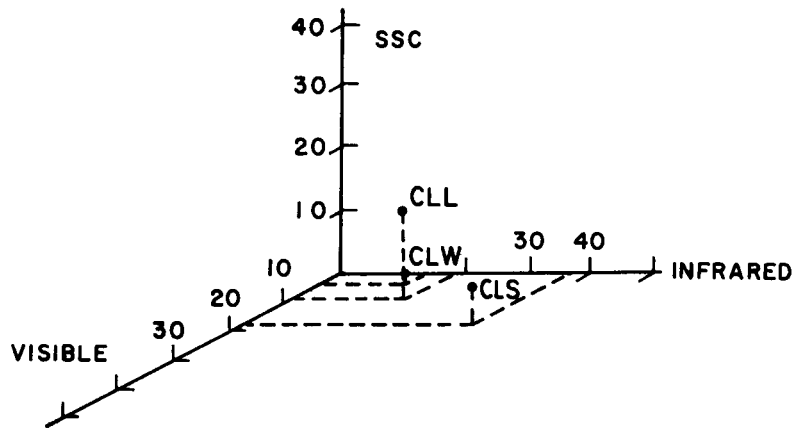


Figure 23. Plots of Category Means in Three Dimensions (SSC, Visible, Infrared). The clear categories are in the upper plot, the water cloud categories are in the middle plot, and the ice cloud categories are in the lower plot

similar to Eq. (8) are discussed in an earlier report<sup>34</sup> and will not be repeated here. Note the similarity between Eq. (8) and Eq. (7).

Finally, the unnormalized classifier with standard deviations is defined by the following:

$$g_i(x, s) = ||x - \mu_i|| + ||s - \Sigma_i||, \quad i = 1, 2, 3, \dots, 9, \quad (9)$$

where  $i$ ,  $x$ ,  $\mu_i$ , and  $|| \quad ||$  are as previously defined,  $s$  is a 3-component column vector  $\begin{pmatrix} s_1 \\ s_2 \\ s_3 \end{pmatrix}$  whose components are the case visible ( $s_1$ ), IR ( $s_2$ ), and SSC ( $s_3$ ) standard deviations;  $\Sigma_i$  is the mean of all  $s$ , category  $i$  with components  $\sigma_n^i$ . Rewriting Eq. (9) as was Eq. (6), we get

$$g_i(x, s) = \sum_{n=1}^3 \left[ (x_n - \mu_n^i)^2 + (s_n - \sigma_n^i)^2 \right], \quad i = 1, 2, 3, \dots, 9. \quad (10)$$

A  $g_i$  is calculated for all  $i$  and category  $k$  is chosen such that  $g_k < g_i$  for all  $i \neq k$ .

Equation (10) differs from Eq. (7) by the factor  $\sum_{n=1}^3 (s_n - \sigma_n^i)^2$ . This classifier was tested to see how well it helps discriminate among cloud categories when  $x$  is "close" to more than one characteristic vector  $\mu_i$ . For example, when  $x$  is equally (or nearly equally) close to two mean vectors  $\mu_i$  and  $\mu_k$ , the choice made by Eq. (10) will favor the cloud category whose standard deviations most closely resemble the visible, IR, and SSC standard deviations of the case. This is potentially helpful for successful discrimination of clear land from cumulus with a water background, clear water from cirrus with a water background, or cumulus with a water background from cirrus with a land background, since the mean of any of these cloud categories can be very similar to one of the others. However, their standard deviations are dissimilar. Such decisions are critically important since cloud/no cloud and phase identification errors result when misclassifications by Eq. (7) occur.

In order to provide a yardstick to measure the improvements offered by adding the SSC channel, the decision rule in Figure 24 was prepared. Only IR and visible means are used. The boundaries between clear, ice cloud, and water cloud were drawn after inspecting scattergrams of cases in the IR/visible plane. No region was drawn for snow or ice cover since to do so would have caused more misclassifications of clouds as snow than correct classifications of snow as snow.

34. d'Entremont, R. P. (1980) Performance of the Discrete Fourier Transform Satellite Imagery Classification Technique, AFGL-TR-80-0175, ADA 095364.

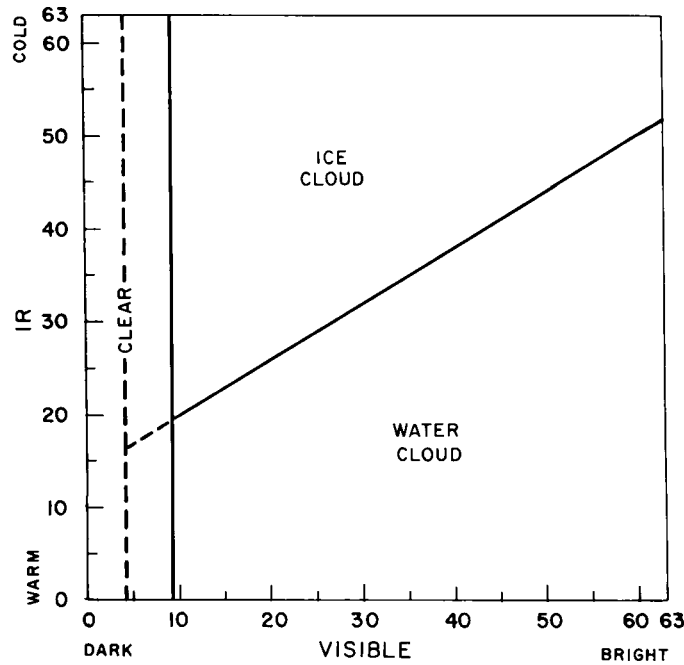


Figure 24. Decision Matrix for Visible and IR Data. The solid lines are used for land backgrounds while the dashed lines are extensions for water backgrounds

The algorithms for automated cloud classification that have been introduced in this section can all be described and compared in the formal terminology of pattern classification and scene analysis. Duda and Hart<sup>33</sup> describe the common elements of pattern classification systems as a transducer, which views the scene and provides raw data; a feature extractor, which derives significant parameters for pattern discrimination; and a classifier, which yields a decision as to what categories are in the scene. In our study, the transducer consists of the SSC and OLS sensors; the feature extractor consists of the software for colocation, normalization, and computation of means and standard deviations; and the classifiers are the various algorithms to make clear/cloud and ice cloud/water cloud decisions.

The problem of classification is basically one of partitioning the feature space into regions, one region for each category, with a minimum of wrong decisions. In our case the feature space is generally the 3-dimensional (3D) space with coordinates of SSC, visible, and IR greyscale (Figure 23). In the case of the minimum distance classifier with standard deviations, a 6-dimensional space (6D) is implied, although two 3D spaces are actually defined. A critical threshold of one spectral channel, for example SSC = 10, defines a plane which is the boundary of two regions in the space. The use of thresholds for two or three channels generates regions like

rectangles or blocks, respectively. A critical ratio such as SSC/visible = 0.7 is a slanted plane which extends from, but does not include, the IR axis. The use of two or more ratios generates wedge-shaped regions. A person, guided by the data, can arbitrarily draw the boundaries of regions. Woronicz<sup>3</sup> has done this, and we have done it for IR and visible data only. Finally, the boundaries of regions may be calculated using discriminant functions such as the distance of points to class means. These boundaries are expected to be non-linear and to reflect the positions of the class means.

## 6. RESULTS

The cases selected and identified by image analysis were used to find ratios, thresholds, and statistics needed by the automated classifiers. For each of the 433 cases, the mean visible brightness count was computed:

$$x_{\text{Vis}} = \frac{\sum_{i=1}^{16} a_i}{16} , \quad (11)$$

where the  $a_i$  are the members of the 16-element visible case array. Similarly  $x_{\text{IR}}$  and  $x_{\text{SSC}}$  were also computed as follows:

$$x_{\text{IR}} = \frac{\sum_{i=1}^{16} b_i}{16} , \quad (12)$$

$$x_{\text{SSC}} = \frac{\sum_{i=1}^{16} c_i}{16} , \quad (13)$$

where  $b_i$  and  $c_i$  are elements of the IR and SCC case arrays, respectively. Note that  $x_{\text{Vis}}$ ,  $x_{\text{IR}}$ , and  $x_{\text{SSC}}$  are the same as  $x_1$ ,  $x_2$ , and  $x_3$  respectively in Eq. (6). The case variances were also computed:

$$s_{\text{Vis}}^2 = \sum_{i=1}^{16} \frac{(a_i - x_{\text{Vis}})^2}{16} , \quad (14)$$

$$s_{IR}^2 = \sum_{i=1}^{16} \frac{(b_i - x_{IR})^2}{16}, \quad (15)$$

and

$$s_{SSC}^2 = \sum_{i=1}^{16} \frac{(c_i - x_{SSC})^2}{16}. \quad (16)$$

Note that  $s_{Vis}$ ,  $s_{IR}$ , and  $s_{SSC}$  are the same as  $s_1$ ,  $s_2$ , and  $s_3$ , respectively in Eq. (9). The ratio

$$r = \frac{x_{SSC}}{x_{Vis}} \quad (17)$$

was also computed.

These results were sorted by category and background type. Then the following overall statistics were computed:

Overall Category Mean:

$$\mu_{Vis}^k = \sum_{i=1}^{N_k} \frac{x_{Vis,i}^k}{N_k}, \quad k = 1, 2, 3, \dots, 9, \quad (18)$$

$$\mu_{IR}^k = \sum_{i=1}^{N_k} \frac{x_{IR,i}^k}{N_k}, \quad k = 1, 2, 3, \dots, 9, \quad (19)$$

$$\mu_{SSC}^k = \sum_{i=1}^{N_k} \frac{x_{SSC,i}^k}{N_k}, \quad k = 1, 2, 3, \dots, 9, \quad (20)$$

for all case means  $x_{Vis,i}^k$ ,  $x_{IR,i}^k$ ,  $x_{SSC,i}^k$  that are of category  $k$ , and  $N_k$  is the number of cases of category  $k$  [note that  $\mu_{Vis}^k$ ,  $\mu_{IR}^k$ , and  $\mu_{SSC}^k$  are the same as  $\mu_1^i$ ,  $\mu_2^i$ , and  $\mu_3^i$  respectively in Eq. (6)];

Variance of the Means:

$$VOM_{Vis}^k = \sum_{i=1}^{N_k} \frac{(x_{Vis,i}^k - \mu_{Vis}^k)^2}{N_k}, \quad k = 1, 2, 3, \dots, 9, \quad (21)$$

$$VOM_{IR}^k = \sum_{i=1}^{N_k} \frac{(x_{IR,i}^k - \mu_{IR}^k)^2}{N_k}, \quad k = 1, 2, 3, \dots, 9, \quad (22)$$

$$VOM_{SSC}^k = \sum_{i=1}^{N_k} \frac{(x_{SSC,i}^k - \mu_{SSC}^k)^2}{N_k}, \quad k = 1, 2, 3, \dots, 9, ; \quad (23)$$

Category Average Variance:

$$(\sigma_{Vis}^k)^2 = \sum_{i=1}^{N_k} \frac{(s_{Vis,i}^k)^2}{N_k}, \quad k = 1, 2, 3, \dots, 9, \quad (24)$$

$$(\sigma_{IR}^k)^2 = \sum_{i=1}^{N_k} \frac{(s_{IR,i}^k)^2}{N_k}, \quad k = 1, 2, 3, \dots, 9, \quad (25)$$

$$(\sigma_{SSC}^k)^2 = \sum_{i=1}^{N_k} \frac{(s_{SSC,i}^k)^2}{N_k}, \quad k = 1, 2, 3, \dots, 9, \quad (26)$$

where  $(s_{Vis,i}^k)^2$ ,  $(s_{IR,i}^k)^2$ ,  $(s_{SSC,i}^k)^2$  are all variances of category  $k$ , as previously defined in Eqs. (14)-(16). Note  $\sigma_{Vis}^k$ ,  $\sigma_{IR}^k$ , and  $\sigma_{SSC}^k$  are the same as  $\sigma_1^i$ ,  $\sigma_2^i$ , and  $\sigma_3^i$ , respectively in Eq. (8).

For the cloud categories,  $\mu_n^k$ ,  $VOM_n^k$ , and  $(\sigma_n^k)^2$  were calculated separately for cases with land backgrounds and for cases with water backgrounds, as well as for land and water backgrounds together (henceforth called combined cases). The results are in Table 11.

Overall means from Table 11 are plotted in Figures 25 to 30 for the visible-SSC, IR-SSC, and visible-IR planes. Figure 25 has the overall visible and SSC means  $\mu_{Vis}^k$  (Eq. (18)) and  $\mu_{SSC}^k$  (Eq. (20)) for combined cases of each cloud category, in addition to the clear categories. The abbreviation for each category is plotted where the overall category means lie on the plane. The bars extending from the abbreviations are equal in length to  $\sigma_n^k$  (Eq. (24)-(26)), category  $k$ 's overall average standard deviation. In other words, these bars show the average range of scatter from its mean for a  $4 \times 4$  case of that category. If this range of scatter is smaller than the letters, no bars are drawn. The partly cloudy

Table 11. Average Statistics

Category	Bkgnd	No. of Cases	VISIBLE			INFRARED			SSC		
			Mean $\mu$	Variance of Mean VOM	Variance $\sigma^2$	Mean $\mu$	Variance of Mean VOM	Variance $\sigma^2$	Mean $\mu$	Variance of Mean VOM	Variance $\sigma^2$
CLW	Water	61	2.56	0.33	0.06	14.30	11.28	0.20	1.08	0.50	0.15
CLL	Land	85	7.90	0.82	0.50	18.44	37.64	0.50	13.25	9.28	2.50
CLS	Snow	36	19.30	23.55	11.76	37.62	15.98	0.39	5.91	4.04	1.46
ST	Land	23	39.40	22.87	5.41	27.59	39.11	0.54	42.27	36.84	5.59
	Water	23	35.79	25.81	14.11	25.68	46.01	1.46	38.53	45.10	9.69
	Both	46	37.59	27.60	9.76	26.63	43.47	1.00	40.40	44.46	7.64
SC	Land	9	26.13	31.54	30.28	26.88	24.81	3.35	31.21	74.44	21.01
	Water	40	25.82	16.58	50.34	23.10	21.80	3.77	27.54	27.55	34.77
	Both	49	25.88	19.34	46.65	23.79	24.50	3.69	28.21	38.19	32.24
CU	Land	40	16.72	16.34	13.62	16.67	7.30	1.57	18.96	18.84	10.61
	Water	41	12.34	12.64	41.72	16.52	4.69	3.36	12.10	17.81	32.46
	Both	81	14.50	19.26	27.84	16.59	5.98	2.48	15.49	30.07	21.67
CI	Land	8	14.23	17.43	11.31	28.59	39.52	30.06	14.77	13.00	6.00
	Water	26	10.89	17.96	22.47	25.70	30.43	44.57	7.11	11.67	7.82
	Both	34	11.68	19.84	19.84	26.38	34.07	41.16	8.91	22.55	7.39
CS	Land	6	27.01	76.64	13.03	45.05	63.67	9.67	17.90	5.79	2.86
	Water	16	20.46	112.99	10.10	37.57	98.75	13.03	12.87	17.02	3.67
	Both	22	22.25	111.58	10.90	39.61	100.27	12.11	14.24	18.97	3.45
CB	Land	3	53.76	31.48	21.46	56.88	31.95	9.33	17.14	1.12	2.50
	Water	16	50.40	80.30	21.46	57.07	33.20	8.95	16.96	14.54	2.64
	Both	19	50.93	74.10	21.46	57.04	33.01	9.01	16.99	12.43	2.62

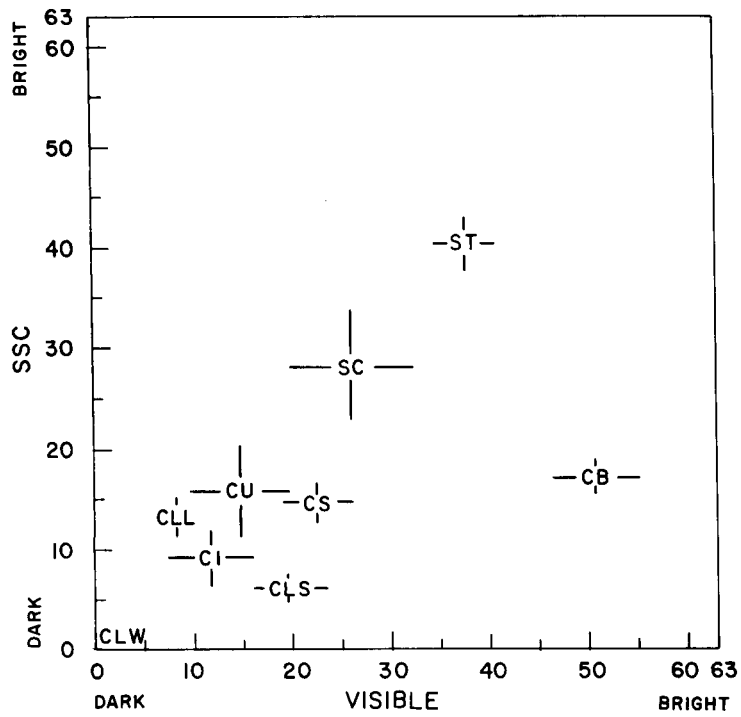


Figure 25. Category Means (Overall Means of SSC and Visible). The bars extending from the category symbols are the overall average standard deviations. If the bars are smaller than the category symbols, they are not drawn. Land and water cases are combined

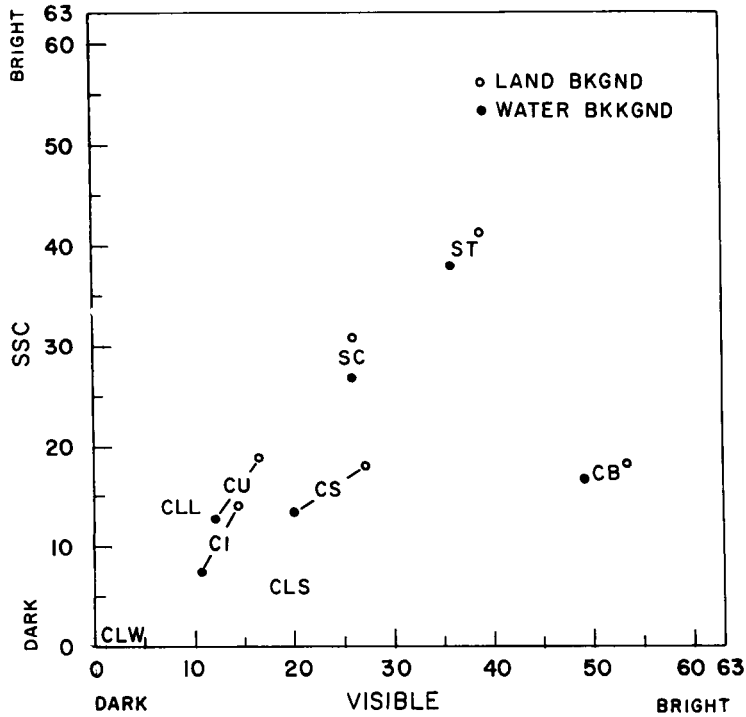


Figure 26. Overall Means of SSC and Visible for Cases Over Water (Dark Circles) and for Cases Over Land (Open Circles)

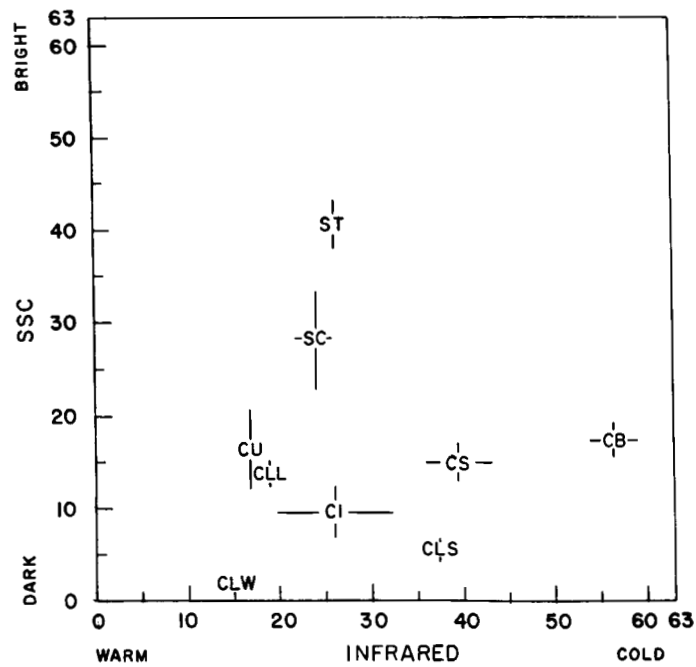


Figure 27. Overall Means and Overall Average Standard Deviations of SSC and Infrared. Land and water cases are combined

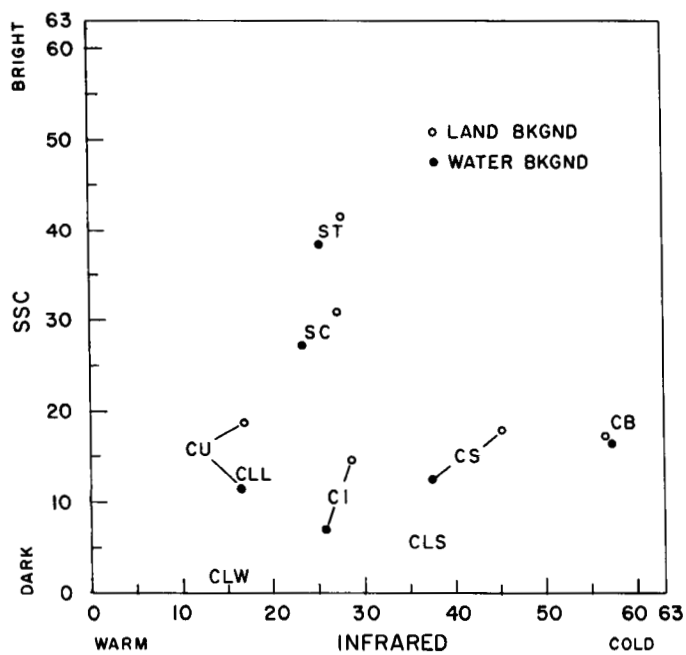


Figure 28. Overall Means of SSC and Infrared for Cases Over Water (Dark Circles) and for Cases Over Land (Open Circles)

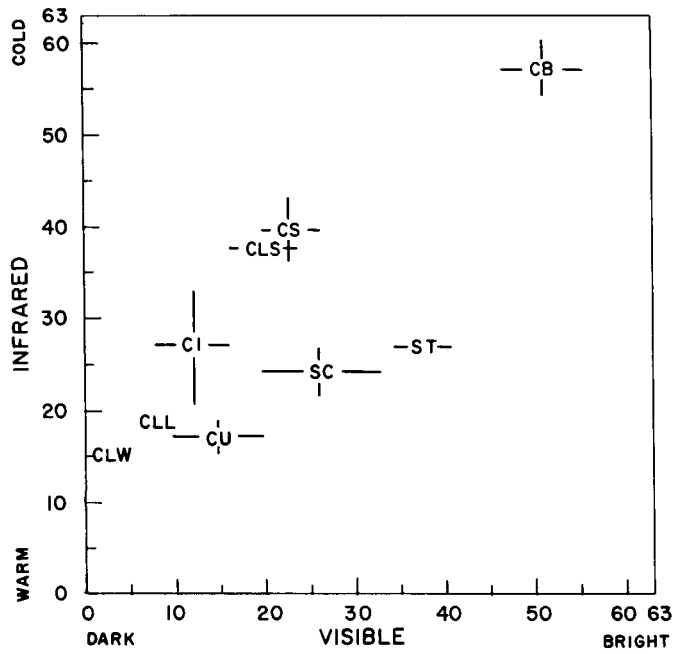


Figure 29. Overall Means and Overall Average Standard Deviations of Infrared and Visible. Land and water cases are combined

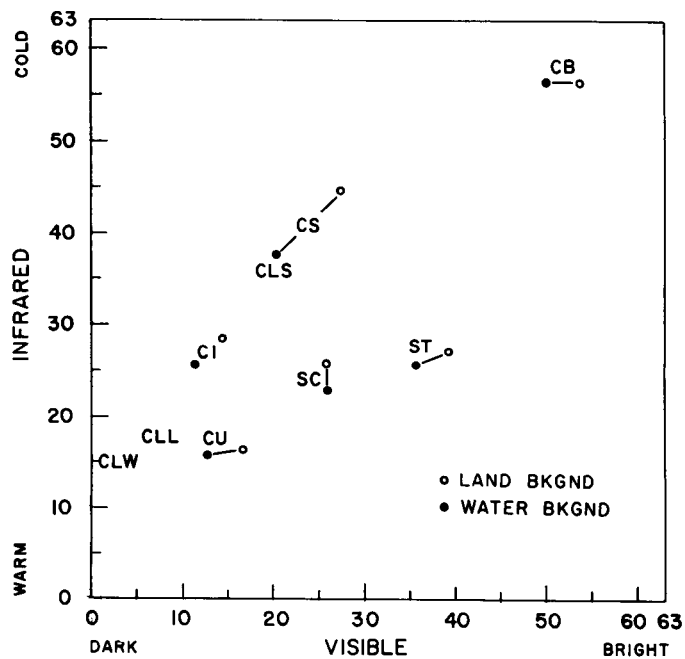


Figure 30. Overall Means of Infrared and Visible for Cases Over Water (Dark Circles) and for Cases Over Land (Open Circles)

categories CI, CU, and SC have the largest bars, as expected, since each  $4 \times 4$  case array has a mixture of clear and cloudy pixels by our image analysis rules. Simple inspection of Figure 25 suggests that, if only SSC and visible data are available, these three categories (CI, CU, and SC) would be hardest to classify since their overall means are closest and vary the most. The overall average standard deviations of each category are different enough to suggest their use as classification features since they discriminate CU from CLL and CI from CLS.

Figure 26 has overall means for cases over water (dark circles) and for cases over land (open circles). The cases over land generally appear brighter, especially for the partly cloudy categories CU and CI. The shifts for both CU and CI make sense since they are similar to the shifts between CLW and CLL. In other words, the land background increases average brightness of the partly cloudy categories. The cloud cases over land (open circles in Figure 26) are more distant from the overall means for clear land and snow than are the cloud cases over water. More distance implies less overlap or higher classification accuracies so it makes sense to use different classifiers for land and water backgrounds. Consequently, we have chosen separate thresholds and statistics for land and water backgrounds in our tests of classifiers. The present 3DNEPH earth-locates all satellite data and labels it by background type at eighth-mesh resolution (about 25 nmi at  $60^\circ\text{N}$ ) to improve cloud/no cloud decisions.

Figures 27 and 28 are like Figures 25 and 26 except that IR replaces visible. In the IR, CLL, CU, SC, ST, and CI have overall means  $\mu_{\text{IR}}^k$  fairly close together. The category average standard deviations,  $\sigma_{\text{IR}}^k$ , are large for the ice clouds CI, CS, and CB and this feature can be used to distinguish CI and CS from CLL and CLS. Figure 28, like Figure 26, shows that the partly cloudy categories have a substantial shift in overall category means as the backgrounds change from water to land. Figures 29 and 30 are plots in the IR-visible plane. CLS is easily confused with CI and CS in this plane since its overall mean is close to the others. CLL is much closer to CLW than in the SSC-visible or SSC-IR planes. CB clouds are well-discriminated from all other categories.

Table 11 shows that the variance of the means (VOM in Eqs. (21)-(23)) is often greater than the category average variance (Eqs. (24)-(26)). In other words, the variation from case to case is often greater than the variation of the 16 elements within a case. For the SSC and visible channels, some of the case-to-case variation is due to cloud reflectivity, some to the fraction of cloud cover, and some to changes in background. For IR data, the variance of the means tends to be high. The cloud cases are expected to vary in temperature, even in the same category, due to differences in cloud altitude or thickness from case to case. The clear cases vary in temperature due to varying background (or clear column) temperatures from Tropics to the Arctic.

Anything that can be done to reduce the variance of the means within a category tends to reduce the overlapping subregions of categories and thereby improve classification accuracy. When independent estimates of clear column temperature are available, as in the 3DNEPH, the IR variance of the means can be reduced for the clear categories and improved clear/cloud decisions are expected. We did not, however, have clear column temperatures in our data base, and all IR values are unadjusted greyscale.

The individual means for each case were all entered on large plots with the same coordinates as Figures 25 to 30. These plots are not reproduced here since they had to be large (about  $1 \text{ m}^2$ ) and use different colors for all the categories. They were, however, more useful than the computed statistics, like variances of the means, in demonstrating how categories would overlap and for selecting critical ratios and boundaries for the automated classifiers.

The yardstick for measuring the extra information provided by the SSC channel is classification rate with only visible and IR data. The decision matrices (one for land, one for water) using visible and IR data were given in Figure 24. These matrices were applied to the 433 cases that were found by image analysis and the resulting verification matrix is given in Table 12. The percentage of hits for 3-way classification was 82.2 percent. The percentage of hits is the percentage of cases correctly classified as either clear (no cloud), ice clouds, or water clouds. The correct cases are found in the diagonal of the matrix from upper left to lower right. The rows in Table 12 give the percentage of observed cases of a particular type as they are classified by the automated classifier. Therefore, the row percentages sum to 100 percent. The numbers in brackets are total numbers of cases for rows and columns. The grand total (433) is also given. This classifier could not be made to work over snow. All the cases of snow were incorrectly identified as ice clouds. If we had cases of pure snow cover without forests, etc., mixed in the scenes, we expect those snow cases would be incorrectly identified as water clouds.

The visible-IR decision matrices did a remarkable job of detecting water clouds (86.4 percent) and ice clouds (82.7 percent) considering that either channel, used by itself, did a poor job of discriminating cloud phase. Ice clouds, for example, were found to have a very broad range of OLS visible reflectivities from 5 to 76 percent. This range is in fact broader than the range of reflectivities for water clouds, which was 7 to 60 percent. Ice clouds were also observed over a broad range of IR temperatures, from  $288^\circ\text{K}$  to  $210^\circ\text{K}$ . (The warmer temperatures were for optically thin cirrus over warm backgrounds.) The visible-IR decision matrices appear to provide useful information as to cloud phase, if the clear/cloud decision is correct and if the decision matrices are not used over areas that may have snow cover or sea ice.

Table 12. Results of Classifier Using Only Visible and IR Data

		Automated			
		Clear	Water Cloud	Ice Cloud	
Observed	Clear	78.0%	2.2%	19.8%	(182)
	Water Cloud	5.1%	86.4%	8.5%	(176)
	Ice Cloud	17.3%	0	82.7%	( 75)
		(164)	(156)	(113)	(433)
(Overall Accuracy 82.2%)					

Two different decision matrices are used: one for land and one for water.

Table 13 summarizes the ratios  $r$  of SSC over visible data which were computed to test ratios for decisions of cloud phase and cloud/snow. Table 13 has values of  $\bar{r}$ , the average of  $r$  [Eq. (17)] over all cases in each category. Clear land had the highest value (1.662) of  $\bar{r}$ . Despite our review of available literature, we were unaware of this important feature to identify clear land until we had seen the results of the SSC experiment. As expected, clear snow has the lowest value (0.312) of  $\bar{r}$ , water clouds have values close to 1.0, and ice clouds have intermediate values. Cumulonimbus clouds have  $\bar{r}$  significantly lower than the other ice clouds. Figure 25 shows that CB has about the same SSC mean but a much higher visible mean, hence the ratio is lower. Clear water had a low  $\bar{r}$  and a discontinuous distribution of  $r$  values between 0 and 1.0. For clear water, the SSC had greyscale from 0 to 2 while the visible had greyscale from 1 to 4, which limits the possible combinations to generate  $r$ . The lowest values of  $r$  for all cases and all categories occurred when the SSC greyscale was zero over clear water.

Following suggestions by scientists at NASA,<sup>10</sup> we limited ratios to those cases with a substantial optical thickness in the visible, which we chose as visible greyscale 9, reflectivity about 11 percent. We recomputed  $\bar{r}$  for these cases, but there was not much change from the  $\bar{r}$  for all cases. We also computed an average  $r$  for each case based on 16 ratios, one for each element of the  $4 \times 4$  arrays. We were concerned that partly cloudy cases might give misleading values of  $\bar{r}$  but we found only small differences in ratios (Table 13).

By trial and error, we found that  $\bar{r} = 0.70$  gave the most accurate decisions for water cloud/ice cloud discrimination. We were not able to find a good  $\bar{r}$  to

Table 13. Ratios of SSC/Visible for Clear and Cloudy Categories

Type	$\bar{r}$	$N_{\text{Vis} > 9}/N_T$	$\bar{r}_{\text{Vis} > 9}$	Average $c_i/a_i$ Vis > 9	
Clear Water (CLW)	0.436	0/61	0	0	
Clear Land (CLL)	1.662	4/85	1.345	1.562	
Clear Snow (CLS)	0.312	36/36	0.331	0.317	
Stratus (ST)	Land	1.088	23/23	1.088	1.092
	Water	1.088	23/23	1.088	1.098
Stratocumulus (SC)	Land	1.206	9/9	1.214	1.259
	Water	1.067	40/40	1.067	1.099
Cumulus (CU)	Land	1.156	40/40	1.153	1.173
	Water	0.983	32/41	0.989	0.946
Cirrus (CI)	Land	1.049	7/8	1.057	1.034
	Water	0.664	16/26	0.663	0.633
Cirrostratus (CS)	Land	0.719	6/6	0.725	0.729
	Water	0.720	14/16	0.689	0.692
Cumulonimbus (CB)	Land	0.326	3/3	0.328	0.324
	Water	0.349	16/16	0.353	0.350

separate ice clouds from clear snow since  $\bar{r}$  for CB (0.326 to 0.349) was close to that of CLS (0.312).

The results of a classifier for no clouds, water clouds, or ice clouds using visible >9 to detect clouds and an SSC/visible ratio of 0.7 to separate the cloud phase is given by Table 14. The overall accuracy of classification is 80.1 percent. The critical ratio was varied in order to maximize the classification accuracy. Most of the mistakes in classification are due to clear snow cases that were classified as ice clouds due to low ratios, clouds over water that had visible greynshades low enough to be classified as clear, and ice clouds with ratios above 0.7 that were classified as water clouds.

This test of the ratio classifier is not entirely fair to investigators who have advocated the use of SSC/visible ratios since we have included an arbitrary clear/cloud decision in the scoring process while the ratios were mainly advocated for detecting cloud phase. Nevertheless, the test is a reasonable simulation of what a satellite data processor must do since a clear/cloud decision must be made before a cloud phase decision can be made.

Table 14. Results of Classifier Using Ratios of SSC/Visible Data

		Automated			
		Clear	Water Cloud	Ice Cloud	
Observed	Clear	78.0%	2.2%	19.8%	(182)
	Water Cloud	5.1%	92.6%	2.3%	(176)
	Ice Cloud	17.3%	26.7%	56.0%	( 75)
		(164)	(187)	( 82 )	(433)
(Overall Accuracy 80.1%)					

The same decision rule is used for land and water backgrounds.

The classification accuracy could be improved in several ways. First, the use of 0.25 as a critical ratio to discriminate snow from ice clouds could improve the accuracy by as much as 5 percent, if many snow cases were classified. (If no snow cases were classified, this procedure would decrease the accuracy since some CB would be classified as CLS.) Also, a category "cloud, phase unknown" could be added and separate classifiers used over land and water backgrounds. Finally, we should note that the ratio approach is expected to work even if SSC and visible data are not normalized for solar angle or anisotropic scattering. Our data sample does not reflect these benefits since both SSC and visible data were normalized for scene solar elevations.

The decision matrices that used only visible and IR data (Figure 24) gave a slightly better classification (82.2 percent) than the ratios classifiers (80.1 percent) that used SSC and visible data. Consequently, more sophisticated decision rules are needed to show how the SSC channel can add information to the OLS visible and IR channels and these rules are shown in the remainder of this section.

The SSC data base enabled us to specify critical thresholds for the classifier proposed by Hunt et al.<sup>4</sup> Also, the use of the thermal channel was changed in order to improve cloud phase discrimination. The revised flowchart is shown in Figure 31. The change in the original flowchart (Figure 20) consists of using a medium range of SSC greyshades to include ice clouds and the water clouds which were not detected by the high SSC threshold. These water clouds were mainly CU. We found high SSC thresholds above which all clouds were water clouds. The thresholds (23 for land and 24 for water cases) correspond to an SSC in-band

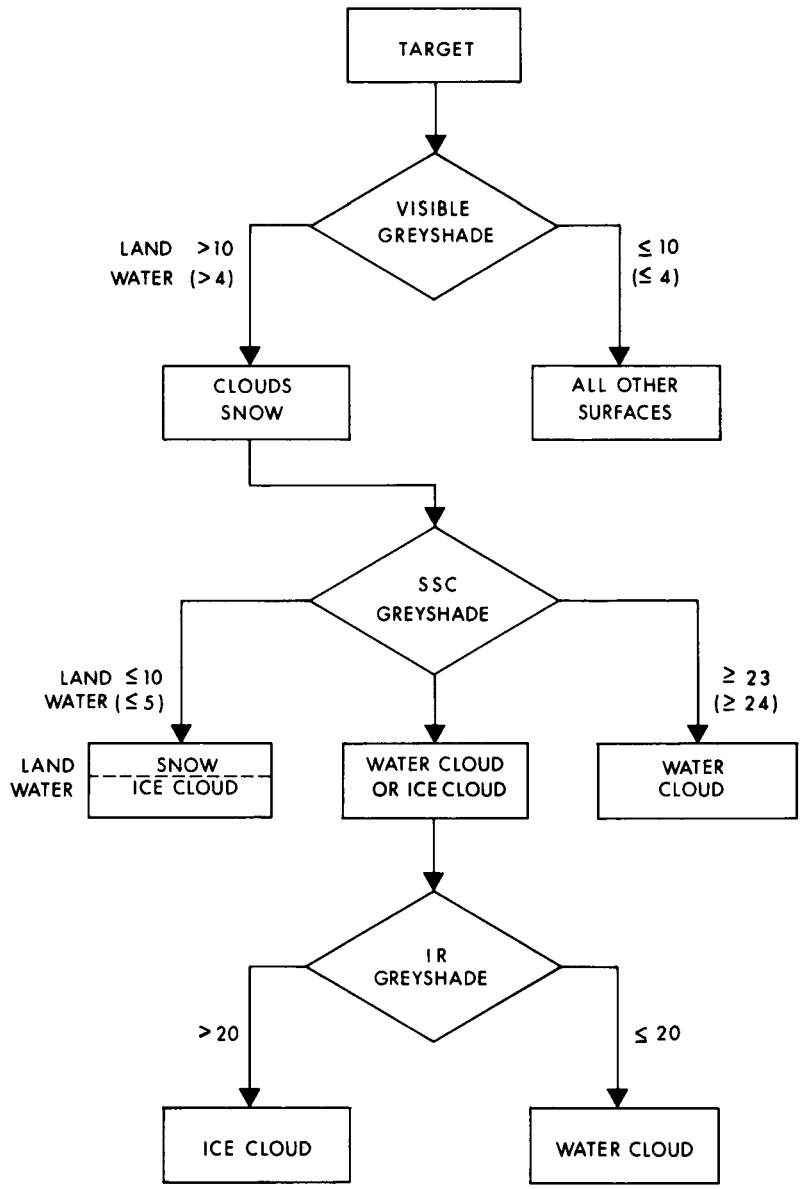


Figure 31. Critical Thresholds and Modification of Hunt Decision Tree Based on Our Cases

reflectivity of about 30 percent. We also found a low SSC threshold (greyscale 10, reflectivity 13 percent) below which all cases over land were snow cover. The IR data was used only to separate the remaining water clouds (mostly CU) from the ice clouds. Over water backgrounds, the low range of SSC greyscales is used to capture the thinnest cases of cirrus clouds over water.

The results of this classifier are impressive (Table 15). The accuracy of classification is 96.1 percent for the four way classification clear, snow, water cloud, or ice cloud. The results are significantly better than the accuracy of the visible-IR classifier that (1) attempted only three categories; (2) had an accuracy of only 82.2 percent (Table 12); and (3) did not work over snow covered land. The results also confirm the predictions of earlier studies that the addition of an SSC channel to the OLS visible and IR can improve cloud detection, discriminate cloud phase, and provide a totally new capability to detect snow cover.

Table 15. Results of Classifier Using SSC, Visible, and IR Data and Adapted From Hunt et al<sup>4</sup>

		Automated				
		Clear	Snow	Water Cloud	Ice Cloud	
Observed	Clear	98.6%	0	0.7%	0.7%	(146)
	Snow	0	100%	0	0	( 36)
	Water Cloud	1.1%	0	93.8%	5.1%	(176)
	Ice Cloud	2.7%	0	2.7%	94.6%	( 75)
		(148)	( 36)	(168)	( 81)	(433)
(Overall Accuracy 96.1%)						

Two different decision rules are used: one for land and one for water backgrounds.

The classifier suggested by Kimball<sup>23</sup> (Figure 21) was also tested with the SSC data base. After examining the data base and ratios (Table 13), we chose KR = 0.70 for decision box (1) to separate clear land and water clouds from other categories and KM = 1.35 for decision box (2) to separate the clear land and water cloud cases. (The value KR = 0.70 was previously used in the ratios approach to discriminate water clouds from ice clouds.) We could not duplicate what Kimball intended for decision box (3) since we did not have  $T_G$ , the clear column IR temperatures. The best we could do was to arbitrarily use IR greyscale 45 (about 240°K) to help discriminate ice clouds such as CB from snow or clear water.

Due to the nature of the algorithm and the fact that it was intended for onboard processing (which might preclude separate processors for land and water backgrounds), we tested only one decision rule for the Kimball approach. The results

are given in Table 16. The overall accuracy for clear/cloud decisions was 82.9 percent. This classification accuracy was essentially the same as the accuracy for the decision matrices that used only visible and IR data, so the misclassified cases were examined to see why the SSC channel was not improving accuracy in this algorithm. For clear cases, all the misclassifications were due to overlaps in the ratio distributions for clear water, water clouds, and clear land categories. Some of the clear water cases had SSC/visible ratios high enough to be called water clouds while some of the clear land cases had ratios low enough to be called water clouds. These misclassifications (12.6 percent, Table 16) could not be improved by choosing different critical ratios KR and KM. For cloudy cases, two-thirds of the misclassified cases (20.3 percent, Table 16) were the partly cloudy categories CI and CU. On the other hand, the Kimball classifier successfully put all snow cases into the clear category. For land backgrounds only, the accuracy improves to 86.2%.

Table 16. Results of Classifier Using SSC, Visible, and IR Data and Adapted From Kimball<sup>2,3</sup>

		Automated		
		Clear	Cloud	
Observed	Clear	87.4%	12.6%	(182)
	Cloud	20.3%	79.7%	(251)
		(210)	(223)	(433)

(Overall Accuracy 82.9%)  
(Land cases only, 86.2%)

The same decision rule is used for land and water backgrounds.

The Woronicz<sup>3</sup> decision matrix (Figure 22) was modified into separate decision matrices for land and water backgrounds. Moreover, the cloudy region was divided into regions for water clouds and ice clouds. The modified decision matrices appear in Figures 32 (land backgrounds) and 33 (water backgrounds). The prime differences in Figures 32 and 33 are the larger size of the clear region for land backgrounds and the ice cloud region for water backgrounds. The ice cloud/water cloud boundary is nearly identical for both decision matrices. This boundary has two segments, a sloping line for the relatively dark clouds and a horizontal line for the brighter clouds. These lines were drawn by hand based on scatter diagrams that positioned all cases. It is important to note that the sloping lines are very

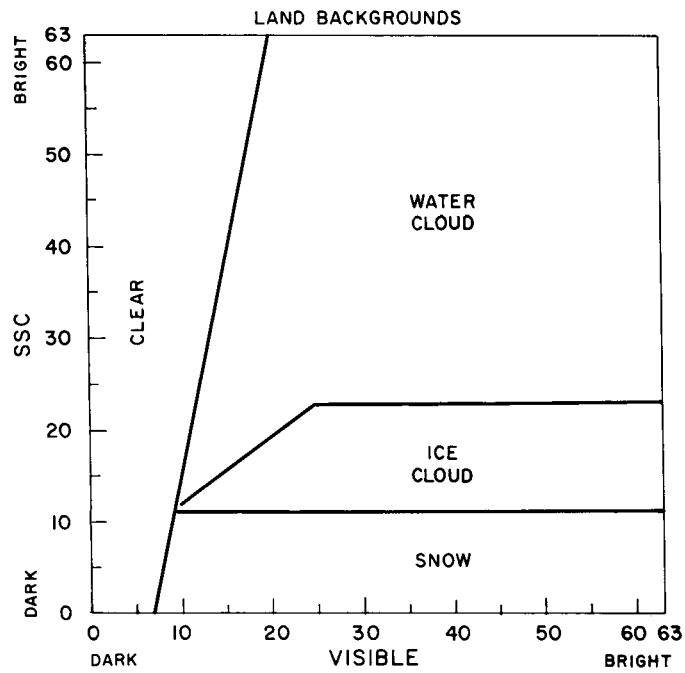


Figure 32. Woronicz Matrix Modified for Land Back-grounds Only with the Cloudy Region Divided into Separate Regions for Water Clouds and Ice Clouds

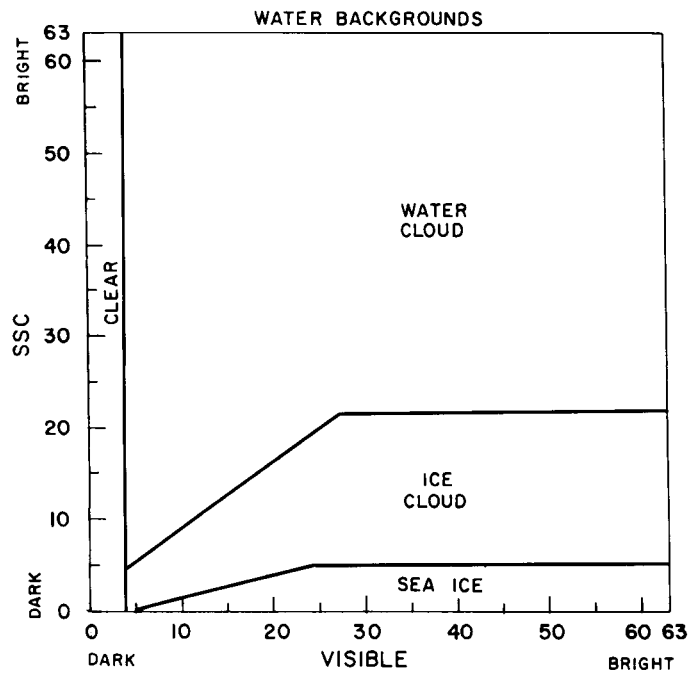


Figure 33. Woronicz Matrix Modified for Water Back-grounds Only with the Cloudy Region Divided into Separate Regions for Water Clouds and Ice Clouds. A region for sea ice is included

close to the line defined by the ratio  $SSC/visible = 0.7$ . However, for the brighter clouds, a constant value of SSC reflectivity (about 30 percent) works best to discriminate cloud phase. This same value of SSC reflectivity was used as a critical threshold in the modified Hunt algorithm. Therefore, the utility of the ratio approach to our data sample is only for discriminating the partly-cloudy water phase categories (CU or SC) from the partly cloudy or semitransparent ice phase categories. The overcast cases are best discriminated by phase using the SSC channel alone.

The results of the modified classifiers are given in Table 17. The results are very good, with an overall classification accuracy of 89.6 percent for four way classification. The majority of the misclassifications are improper phase decisions for the (partly cloudy) categories of CI and CU. These categories are separated by the sloping boundaries in Figures 32 and 33 but there is still some scatter of both CI and CU cases across these sloping boundaries. The cloud phase discrimination in this subregion of the SSC-visible plane could be improved either by using unaveraged rather than  $4 \times 4$  averages of SSC data to better detect the smaller clouds or else by using IR data to distinguish the colder CI clouds from the warmer CU, which was done in the Hunt algorithm. The Woronicz decision matrix in Figure 22, which does not assume prior knowledge of the type of background, was also tested on all the cases (see Table 18).

Table 17. Results of Classifier Using the Woronicz Decision Matrix Modified to Separate Matrices for Land and Water Backgrounds

		Automated				
		Clear	Snow/ Sea Ice	Water Cloud	Ice Cloud	
Observed	Clear	97.9%	0.7%	0.7%	0.7%	(146)
	Snow/ Sea Ice	0	100%	0	0	( 36)
	Water Cloud	1.7%	0	85.2%	13.1%	(176)
	Ice Cloud	2.7%	0	18.7%	78.6%	( 75)
		(148)	( 37)	(165)	( 83)	(433)

(Overall Accuracy 89.6%)

Table 18. Comparison of Classification Accuracies for Woronicz Style SSC-Visible Decision Matrices

	Woronicz Matrix on Woronicz Data		Woronicz Matrix on Our Data		Land/Water Matrices on Our Data		
Classification Categories	Clear	Clear	Clear	Clear	Clear	Clear	Clear
	Cloud	Snow	Cloud	Snow	Cloud	Snow	Snow
		Cloud		Cloud		Cloud	Water Cloud
							Ice Cloud
Accuracy	90.1%	88.7%	88.5%	88.2%	98.4%	98.2%	89.6%

The classification accuracies are summarized in Table 18. The classification accuracies improve when a classifier is used for fewer categories. The improvement is expected since the results of a larger table (for example, Table 17) are combined into a smaller table and some misclassifications become correct classifications. The results of the Woronicz decision matrix on our cases are almost identical to the results on his cases with all accuracies between 88.2 to 90.1 percent. When separate decision matrices are used for land and water backgrounds, the accuracy increases to over 98 percent for two or three categories. When cloud phase discrimination is added, the classification accuracy is still good (89.6 percent) and could easily be improved by a judicious use of the IR temperatures.

The three forms of minimum distance classifiers, which have decision rules defined by Eqs. (7)-(9), were also tested. Separate classifiers were generated for land and water backgrounds. The classification results appear in Tables 19, 20, and 21. The classification accuracies are almost the same for the three forms of classifiers, ranging from 91.5 to 92.6 percent. These results are higher in accuracy than all the other classifiers with the exception of the Hunt decision rules when the classifiers are used for clear/snow/water cloud/ice cloud categories.

The minimum distance classifiers have some advantages over the other classifiers. All three forms of the minimum distance classifiers were excellent for discriminating water clouds from ice clouds. Of all the classifiers tested, the best cloud phase discrimination was done by the minimum distance classifier using normalized means [Eq. (8) and Table 20]. Water clouds were detected at the rate of 94.9 percent while ice clouds were detected at the rate of 97.4 percent. The minimum distance classifiers are also relatively easy to work with when the feature space has more than two dimensions. Using two-dimensional scattergrams,

Table 19. Results of Minimum Distance Classifier Using Unnormalized Means of SSC, Visible, and IR Data [Eq. (7)]

		Automated				
		Clear	Snow	Water Cloud	Ice Cloud	
Observed	Clear	88.4%	0	0.7%	10.9%	(146)
	Snow	0	91.7%	0	8.3%	( 36)
	Water Cloud	2.8%	0	95.5%	1.7%	(176)
	Ice Cloud	9.3%	0	0	90.7%	( 75)
		(141)	( 33)	(169)	( 90)	(433)
(Overall Accuracy 91.9%)						

Two different decision rules are used: one for land and one for water backgrounds.

Table 20. Results of Minimum Distance Classifier Using Normalized Means of SSC, Visible, and IR Data [Eq. (8)]

		Automated				
		Clear	Snow	Water Cloud	Ice Cloud	
Observed	Clear	84.9%	0.7%	0.7%	13.7%	(146)
	Snow	0	88.9%	2.8%	8.3%	( 36)
	Water Cloud	0	0	94.9%	5.1%	(176)
	Ice Cloud	1.3%	0	1.3%	97.4%	( 75)
		(125)	( 33)	(170)	(105)	(433)
(Overall Accuracy 91.5%)						

Two different decision rules are used: one for land and one for water backgrounds.

Table 21. Results of Minimum Distance Classifier Using Unnormalized Means and Standard Deviations of SSC, Visible, and IR Data [Eq. (9)]

		Automated				
		Clear	Snow	Water Cloud	Ice Cloud	
Observed	Clear	90.4%	0.7%	0.7%	8.2%	(146)
	Snow	0	91.7%	0	8.3%	( 36)
	Water Cloud	2.8%	0	96.0%	1.2%	(176)
	Ice Cloud	10.7%	0	0	89.3%	( 75)
		(145)	( 34)	(170)	( 84)	(433)

(Overall Accuracy 92.6%)

Two different decision rules are used, one for land and one for water backgrounds.

category subregions like the Woronicz subregions are easily drawn by hand and converted to replacement tables for the computer, but this approach is not convenient for more than two dimensions.

Six dimensions are used for the feature space for the minimum distance classifier using unnormalized means and standard deviations. The standard deviations of the  $4 \times 4$  arrays for each case were added as features to help discriminate the partly cloudy cases from cloud-free cases. We noted that the standard deviations of cumulus cases over land were much higher than for clear land in both SSC and visible channels while the mean brightnesses of both types of cases were often very close. In the IR channel, the standard deviations of cirrus cases are much higher than for clear snow cases. Table 22 has results when the minimum distance classifier using both means and standard deviations classifies all nine categories used in this study. The overall accuracy for nine categories is 85.2 percent, almost as good as the 92.6 percent (Table 21) accuracy for only four categories.

All of the minimum distance classifiers were handicapped by the fact that IR greyscale were used without reference to clear-column temperatures, which vary significantly from the Equator to high latitudes. The unadjusted greyscale appear scattered along the direction of the IR axis for clear land, snow, and water categories, and also for the partly cloudy categories. The extra scatter generates some misclassifications as clouds for the colder clear and snow cover cases. The reason why the Hunt classifier has better results (96.1 percent) for four category

Table 22. The Same Classifier Used for Table 21 [Minimum Distance Using Un-normalized Means and Standard Deviations, Eq. (9)] Except that Results are Given for all Nine Categories of Clear Surfaces and Clouds

		Automated									
		CLW	CLL	CLS	ST	SC	CU	CI	CS	CB	
Observed	CLW	100.0%	0	0	0	0	0	0	0	0	( 61)
	CLL	0	83.5%	1.2%	0	0	1.2%	14.1%	0	0	( 85)
	CLS	0	0	91.7%	0	0	0	5.6%	2.7%	0	( 36)
	ST	0	0	0	87.0%	13.0%	0	0	0	0	( 46)
	SC	0	0	0	16.3%	77.6%	4.1%	2.0%	0	0	( 49)
	CU	1.2%	4.9%	0	0	4.9%	87.8%	1.2%	0	0	( 81)
	CI	14.7%	2.9%	0	0	0	0	70.6%	11.8%	0	( 34)
	CS	9.1%	0	0	0	0	0	13.6%	59.1%	18.2%	( 22)
	CB	0	0	0	0	0	0	0	5.3%	94.7%	( 19)
		( 69)	( 76)	( 34)	( 48)	( 48)	( 74)	( 43)	( 19)	( 22)	(433)
(Overall Accuracy 85.2%)											

classification than the minimum distance classifiers (91.5 to 92.6 percent) is the fact that the Hunt classifier uses IR selectively for relatively few cases where the SSC and visible data have trouble discriminating cloud phase.

An alternate procedure to improve the cloud phase discrimination for the partly-cloudy categories of cumulus and cirrus is to refer to the cases in the visible-IR plane. After looking at individual cases, we noted that the classifier using only visible and IR data did better than the Woronicz classifier in discriminating cumulus and cirrus cases. We believe that these small-scale clouds were better discriminated by the visible-IR processor since the visible and IR data are precisely colocated by the OLS instrument while the SSC and visible data are only approximately colocated. If the SSC channel were added to the OLS as a third channel, we expect that the SSC-visible classifiers modified from Woronicz would have improved cloud phase discrimination. We also noted that the visible-IR processors made mistakes in phase discrimination that the processors using the SSC channel did not make. Supercooled stratus clouds, for example, were called ice clouds by the visible-IR processors but were called water clouds when the SSC channel was used. These mistakes limit the accuracy of the visible-IR processors for cloud-phase discrimination so that they do not work as well as classifiers using the SSC channel.

The accuracies of all types of classifiers were compared in Table 23 to help summarize the results of automated cloud classification and cloud phase discrimination. The visible-IR classifier, which was the best approach without the SSC channel, showed skill for cloud phase but did not work over snow cover. The ratios and Kimball classifiers, which both relied on SSC/visible ratios, did no better than the visible-IR approach. Aside from the fact that the Kimball classifier worked well over snow cover, we do not advocate their use without further modification and testing. The remaining three classifiers (Hunt, Woronicz, minimum distance) were substantially more accurate than the visible-IR classifier and also demonstrated how the SSC channel can detect snow cover, cloud phase, and improve the discrimination of clear land.

## 7. OPTIONS FOR IMPROVED 3DNEPH

If the SSC channel were added to the DMSP OLS sensor, then the added information of cloud/snow and cloud phase discrimination could be found in several ways. A prime consideration, which was known before the design of the SSC experiment, is the impact of an extra channel on the spacecraft burden of storing the extra data and downlinking it to command readout stations. The data rate would be high since the FOV would be about the same (1.5 nmi) as smoothed visible and IR. Consequently, there has been a concern to learn if the SSC data could be processed by the spacecraft and a compressed message (such as 1 bit: 0 = no cloud, 1 = cloud) stored and transmitted to the readout stations. Of the algorithms we tested, the Hunt classifier and the modified Woronicz classifiers are the most likely candidates for onboard processing due to their simplicity, as well as their accuracy. They could be used for a data compression of 6 bits (SSC greyscale) to 1 bit (clear/cloud) or 2 bits (clear/snow/water cloud/ice cloud). These classifiers both work better if the type of background, land or water, is known independently. In theory, the independent knowledge of backgrounds could be calculated on the ground for coastline crossings as a function of subtrack and scan angle and be uplinked to the satellite. In practice, it would be easier to substitute classifiers which do not assume prior knowledge of the background at the cost of some classification accuracy. The Hunt classifier, for example, dropped from 96.1 to 86.6 percent for clear/snow/ice cloud/water cloud categories when the background was unknown.

If the data from an SSC channel could be transmitted to the AFGWC, more options are available. It would be available for subjective analysis as well as automated analysis. Our experience with image analysis using SSC displays has led us to believe that it often has more contrast than the visible or IR images for separating cloud layers, where one layer is water and the other is ice cloud, or

Table 23. Comparison of Classification Accuracies

	Classifiers							
	Visible, IR Only	Ratios SSC/Visible	Hunt Decision Rules SSC, Visible, IR	Kimball Decision Rule SSC/Visible, IR	Modified Woronicz Matrices	Minimum Distance Classifiers Using Means and Standard Deviations of SSC, Visible, IR		
Classification Categories	Clear	Clear	Clear	Clear	Clear	Clear	Clear Water	
	Water Cloud	Water Cloud	Snow	Cloud	Snow	Snow	Clear Land	
	Ice Cloud	Ice Cloud	Water Cloud	Ice Cloud	Water Cloud	Ice Cloud	Water Cloud	Snow
			Ice Cloud		Ice Cloud		Ice Cloud	ST
								SC
								CU
								CI
							CS	
							CB	
Accuracy	82.2%	80.1%	96.1%	82.9%	89.6%	92.6%	85.2%	

for locating coastlines and other landmarks even though the SSC resolution was coarse. Clouds over snow cover were easy to recognize using the SSC image alone.

Any automated processing of an extra channel such as the SSC would definitely increase computer storage and calculating requirements compared with processing just IR and visible data. We are not able to estimate these requirements since our calculations were made on a different computer system with no current capability to run 3DNEPH codes. We believe, however, that the benefits of adding the SSC channel to the 3DNEPH would be considerable. Along with Woronicz,<sup>3</sup> we have noted that clouds can be detected over snow cover. The 3DNEPH does not process visible data over areas believed to have snow cover, and cloud detection suffers since the thermal contrast between low cloud tops and snow cover is often too weak to detect these clouds. Cloud phase is important new information that could be added to the 3DNEPH. Aside from detecting a cloud and estimating its altitude, the phase of the cloud is the most useful thing to know for support to many AF operations. Detecting water clouds is particularly important since they tend to occur at low altitudes, they tend to have the worst transmission for electro-optical systems, and they are often supercooled causing icing conditions. The SSC channel detects water clouds very well when it is used with the visible channel.

The 3DNEPH program generates intermediate products of background brightness fields and clear-column temperatures. They are needed to account for global variations in visible reflectivity and IR temperature of clear surfaces so that bright deserts in the visible processor and cold Arctic regions in the IR processor are not mistaken for clouds. These brightness and temperature reference fields can improve classifications using the SSC channel in a multispectral classifier since they reduce the overlap of the clear cases and the cloudy cases.

One very important advantage of the classifiers using the SSC channel was the fact that they achieved high classification accuracies over a great range of latitudes and backgrounds without any location-dependent values of background brightness. It was helpful for the SSC channels to have independent knowledge of the type of background, land or water, but they did not have to be given a numerical value of background brightness for each earth location. In order to use visible satellite data in the 3DNEPH, the AFGWC has had to develop considerable software to maintain a background brightness data base. These procedures are described by Fye.<sup>24</sup> This global data base is eighth-mesh and corresponds directly to the 3DNEPH grid system. The data base is updated daily so that sudden changes in snow fall or snow melting can be followed as well as seasonal changes in vegetation.

The AFGWC maintains a background brightness data base and processes visible data only for sensors on spacecraft with a near-noon (local time) orbit. Visible data are not processed for morning orbits since changes in scene illumination

make it difficult to establish background brightness fields. During the wintertime, for example, the day-to-day variation in the morning pass time will cause locations to be sunlit on some mornings, but dark on others when the satellite passes at an earlier local time. A good background brightness field, which needs daily checks, cannot be established for these conditions. On the other hand, the use of an SSC channel in conjunction with the visible is expected to work in the sunlit parts of a morning orbit since the multichannel classifiers perform well without a background field. However, we cannot say how much of the morning orbit could be processed since we did not use cases close to the terminator ( $SSE = 0^\circ$ ). We did use cases with  $SSE = 15^\circ$  without difficulty and expect that appropriate gain settings would allow automated processing for lower SSE.

The SNODEP<sup>31</sup> model is used to tell the background brightness data base when snow or ice backgrounds are present. The visible data are not used to detect snow or else persisting cloud cover could be identified as snow cover. The use of an SSC channel along with the visible channel would allow snow cover to be detected as well as cloud cover so that the SNODEP data base could be improved for regions where snow cover reports are sparse.

The combination of processing some visible data from morning orbits, as well as over snow cover on both morning and noon orbits, could substantially increase the automated processing of visible data. Therefore, an important feature of the SSC channel is that it allows much more data from the visible channel to be used in the 3DNEPH.

## 8. CONCLUSIONS

Before the data from the near-IR SSC channel were available, there were a number of questions to be answered despite the available literature. Not all backgrounds and cloud types had been observed in previous studies; however, the polar-orbiting DMSP satellite carried the SSC over a variety of backgrounds and cloud types not previously observed. Earlier measurements showed that cloud-free land had a higher reflectivity than the broadband OLS visible channel, and these bright backgrounds might be difficult for cloud detection. On the other hand, both our study and the Woronicz<sup>3</sup> study found minimum problems in cloud detection as long as the visible channel was included and a multispectral approach was used. The clear land cases were in a unique region of the SSC-visible plane and were characterized by the highest values of the ratio SSC/visible of all the cases. This important finding was not predicted in the literature available to us, but it is very useful since clear land, clouds, and snow cover cases are well separated in the SSC-visible plane.

Calculations of cloud reflectivity were useful for predicting the SSC response to clouds. However, the applications of calculations are limited by the great irregularities of shape and size of ice particles so that experimental evidence is desirable. We found that the ice cloud cases had a relatively narrow range of reflectivity about an average of 22 percent when the ice clouds were thick. They never appeared as dark as a snow cover (8 percent). Moreover, the presence of a thin ice cloud over a very dark background such as an ocean or snow cover would make the scene brighter, but not so bright as a thick ice cloud. We interpret these observations in terms of the differing scattering properties of ice clouds and snow cover. Aircraft observations<sup>12</sup> of ice clouds show that the uppermost parts of all ice clouds have smaller ice particles than are found in a snow cover. Therefore, the upper parts of ice clouds are more efficient in scattering than a snow cover. The snow cover, in addition to having larger particles, also tends to have a much larger absorbing mass than the ice clouds. These scattering properties help the classifiers to discriminate ice clouds from snow cover.

The variety of cloud types and backgrounds observed in the SSC, visible and IR channels allowed us to test previously suggested classifiers for cloud detection and cloud phase as well as some minimum distance classifiers over global extremes. We found that classifiers relying on the SSC/visible ratio, were not significantly better in overall accuracy than the best classifiers using visible and IR data. We found that the SSC data helped three types of classifiers (Woronicz/AFGWC; Hunt et al; minimum distance classifiers) to achieve accuracies over 90 percent, which were 10 to 16 percentage points better than the best reference classifiers using only visible and IR data. In other words, these three classifiers made only one-half to one-third as many mistakes as the visible-IR classifiers due to improvements in cloud phase detection as well as snow cover detection.

The classifiers had some difficulties with the partly cloudy categories of cumulus and cirrus. We believe that these difficulties would be reduced if the OLS channel had the same FOV as the visible and IR channels. It would be helpful to reference a finer scale (1.5 or 0.3 nmi) of visible and IR for these clouds, but such data were not available for this study.

For four categories (clear, snow, water cloud, and ice cloud) there is no need for more complex algorithms since some classifiers already work well. An increase in complexity leads to an increase in computer time, but may not yield a worthwhile increase in accuracy. We do, however, advocate the use of the IR clear-column temperature fields maintained by AFGWC to increase the utility of IR in the multispectral processors. We also advocate tests of the algorithms on finer scales of future SSC data to improve estimates of fractional cloud cover.

We agree with the conclusions presented by Woronicz,<sup>3</sup> and we encourage readers who are interested in this subject matter to read his report. In particular,

we agree that the SSC channel should be used as part of a multispectral algorithm, which can be used to discriminate clear, cloudy, and snow cover scenes with accuracy. We found that his decision rule for clouds could be easily modified to separate water clouds from ice clouds, and that classification accuracies improve when the data are earth-located so that the type of background, land or water, is known.



## References

1. Valovcin, F.R. (1976) Snow/Cloud Discrimination, AFGL-TR-76-0174, ADA 032385.
2. Valovcin, F.R. (1978) Spectral Radiance of Snow and Clouds in the Near Infrared Spectral Region, AFGL-TR-78-0289, ADA 063761.
3. Woronicz, R. C. (1981) Results of AFGWC Snow Cloud Discrimination Study, AFGWC Technical Note 81-003. (To be published.)
4. Hunt, G.R., Salisbury, J.W., and Bunting, J. T. (1974) Distinction Between Snow and Cloud in DMSP Satellite Imagery, Report to the Fourth AFCRL/AWS Satellite Working Group, 15 pp.
5. Blau, H.H., Jr., Espinola, R. P., and Reifenstein, E. C., III (1966) Near infrared scattering by sunlit terrestrial clouds, Applied Optics 5(No. 4): 555-564.
6. Irvine, W.M., and Pollack, J.B. (1968) Infrared optical properties of water and ice spheres, Icarus 8:324-360.
7. Selby, J.E.A., and McClatchey, R.A. (1975) Atmospheric Transmittance From 0.25 to 28.5  $\mu$ m: Computer Code Lowtran 3, AFCRL-TR-75-0255, ADA 017734.
8. Blau, H.H., Jr., and Hovis, W.A. (1971) Cloud characteristics from infrared measurements, Space Research XI, Akademie-Verlag, Berlin, pp. 731-739.
9. Alishouse, J. C., Jacobowitz, H., and Wark, D.Q. (1976) A Cloud Physics Investigation Utilizing Skylab Data, Final Report to Johnson Space Center, Houston, Texas.
10. Kyle, H.L., Curran, R.J., Barnes, W.L., and Escoe, D. (1978) A Cloud Physics Radiometer, Proceedings of the 3rd Conf. on Atmospheric Radiation, Davis, California, p. 107.
11. Barnes, J. C., Smallwood, M. D., and Cogan, J. L. (1975) Study to Develop Improved Spacecraft Snow Survey Methods Using Skylab/EREP Data, ERT Document No. 0412-F, Final Report, Contract No. NAS9-13305, Environmental Research & Technology Inc., Concord, Massachusetts, 92 pp.

12. Bunting, J. T. (1980) Sensing Ice Clouds From Satellites, Light Scattering by Irregularly Shaped Particles, (D. W. Schuerman, ed.) Plenum Press, New York, p. 25.
13. Twomey, S., and Seton, K. J. (1980) Inferences of clouds from spectral reflectance measurements, J. Atmos. Sci. 37:1065-1069.
14. Wiscombe, W. J., and Warren, S. G. (1981) A model for the spectral albedo of snow, J. Atmos. Sci. 37:2712-2733.
15. Conover, J. H., and Bunting, J. T. (1977) Estimates From Satellites of Weather Erosion Parameters for Reentry Systems, AFGL-TR-77-0260, ADA 053654.
16. Plank, V. G. (1978) Weather Documentation for ANT-II, Launched 4 July 1978, AFGL 60 Day Report.
17. Hobbs, P. V. (1974) Ice Physics, Clarendon Press, Oxford.
18. O'Brien, H. W., and Munis, R. H. (1975) Red and Near Infrared Spectral Reflectance of Snow, ERP No. 332, U.S. Army Cold Regions and Engineering Laboratory, Hanover, New Hampshire.
19. Goetz, A. F. H., and Rowan, L. C. (1981) Geologic remote sensing, Science 211(No. 4484):781-791.
20. Rowan, L. C., Goetz, A. F. H., and Ashley, R. P. (1977) Geophysics 42:522.
21. Anderson, A. G. (1976) Resource and Environmental Surveys From Space With The Thematic Mapper in the 1980's, Report of the National Research Council Committee on Remote Sensing Programs.
22. Nelgner, H. D., and Thompson, J. R. (1962) Airborne Spectral Radiance Measurements of Terrain and Clouds, Emerson Electric of Saint Louis, Report No. 1323 (RPA 6-62).
23. Kimball, A. W. (1980) Technical Operating Report, SSC Data Evaluation, Westinghouse Electric Corporation, Defense and Electronic Systems Center, Baltimore, Maryland.
24. Fye, F. K. (1978) The AFGWC Automated Cloud Analysis Model, AFGWC Technical Memorandum 78-002.
25. Fett, R. W., and Bohan, W. A. (1980) Navy Tactical Application Guide, Volume 3, NAVENVPREDRSCHFAC Technical Report 80-07 (pp. 1A20 to 1A22).
26. Ruff, I., and Gruber, A. (1975) Graphical Relations Between a Satellite and a Point Viewed Perpendicular to the Satellite Velocity Vector (Side Scan), NOAA Technical Memorandum NESS 65.
27. The Times Atlas of the World, Mid-Century Edition (1957) The Americas, Vol. 5, Houghton Mifflin Co., Boston.
28. U.S. Department of the Interior (1970) The National Atlas of the U.S.A., Geological Survey, Washington, D. C.
29. Department of Mines and Technical Surveys (1957) Atlas of Canada, Geographical Branch, Ottawa, Canada.
30. Curran, R. J., and Wu, M-L. (1981) Identification from space of water droplet clouds at temperatures below  $-40^{\circ}\text{C}$ , J. Atmos. Sci. (in press).
31. Luces, S. A., Hall, S., and Martens, J. (1975) The AFGWC Snow Cover Analysis Model, AFGWC Technical Memorandum 75-1.
32. Bunting, J. T., and Fournier, R. F. (1980) Tests of Spectral Cloud Classification Using DMSP Fine Mode Satellite Data, AFGL-TR-80-0181, ADA 094119.

33. Duda, R.O., and Hart, P.E. (1973) Pattern Classification and Scene Analysis, John Wiley & Sons, New York.
34. d'Entremont, R.P. (1980) Performance of the Discrete Fourier Transform Satellite Imagery Classification Technique, AFGL-TR-80-0175, ADA 095364.